PHYSICAL REVIEW D **107,** 055041 (2023)

# Constraining new physics with possible dark matter signatures from a global CKM fit

Aritra Biswas,[*] Lopamudra Mukherjee,[†] and Soumitra Nandi[‡]
*Department of Physics, Indian Institute of Technology Guwahati, Assam 781039, India*

Sunando Kumar Patra[§]
*Department of Physics, Bangabasi Evening College,*
*19 Rajkumar Chakraborty Sarani, Kolkata, 700009, West Bengal, India*

(Received 7 August 2022; accepted 3 March 2023; published 27 March 2023)

We constrain the parameters of a representative new physics model with a possible dark matter (DM) signature from a global Cabibbo-Kobayashi-Maskawa (CKM) fit analysis. The model has neutral quark current interactions mediated by a scalar, impacting the semileptonic and purely leptonic meson decays at one loop. We take this opportunity to update the fit results for the Wolfenstein parameters and the CKM elements with and without a contribution from the new model using several other updated inputs. In addition, we analyze and include the $B \to D^* \ell \nu_\ell$ decay in the CKM fit. The newly available inputs on the relevant form factors from lattice calculations are included, and the possibility of new physics effects in $B \to D^* \ell \nu_\ell$ is considered. We obtain tight constraints on the relevant new physics parameters. We study the possible implications of this constraint on DM phenomenology. Apart from DM, the bounds are also applicable in other relevant phenomenological studies.

DOI: 10.1103/PhysRevD.107.055041

## I. INTRODUCTION

The Standard Model of particle physics (SM) has emerged through theoretical and experimental discoveries, and has been tested extensively. Flavor physics has played an essential role in this development. Despite these successes, the SM fails to explain some key aspects of nature. For example, it cannot provide a candidate for dark matter (DM), nor can it accommodate the observed baryon asymmetry. Therefore, extensions of the SM are formulated that address these issues by introducing new degrees of freedom beyond the SM. New particles or interactions introduced at a high scale could have a related shorter-distance interaction. The low-energy observables will hence be useful in constraining the new physics (NP) parameter spaces. In the near future, they might play an essential role in the indirect detection of the new particles through deviations from the respective SM predictions.

The quark mixing matrix, also known as the Cabibbo-Kobayashi-Maskawa (CKM) matrix, is important for understanding *CP* violation. The CKM matrix is a $3 \times 3$ matrix, and precise knowledge of the corresponding elements is essential. Following the Wolfenstein parametrization, four parameters are needed to define all of the elements of the CKM matrix. Therefore, one of the important goals of the flavor studies is to constrain these four parameters using all of the available measurements that are directly or indirectly sensitive to the CKM matrix.

In the SM, the charged-current interactions are the only flavor changing processes that occur at tree level, and the decay rates are directly sensitive to the square of the CKM elements. On the other hand, the flavor-changing neutral-current (FCNC) processes are loop suppressed in the SM, and the corresponding amplitudes are sensitive to the product of CKM elements. Due to their simple and constrained structure in the SM, the weak processes are potentially sensitive to new interactions beyond the SM and hence can be a potent probe for models beyond the SM. It is necessary to measure the CKM parameters very precisely, and during the last few decades extensive research has been performed at the *BABAR*, Belle, and LHCb experiments. High-luminosity experiments like Belle-II have also become operational, and within a few years we expect a wealth of precise data which will be useful to constrain NP model parameters. This paper will consider one such model that contributes to the semileptonic and purely leptonic

---

[*] iluvnpur@gmail.com
[†] mukherjeelopa@iitg.ac.in
[‡] soumitra.nandi@iitg.ac.in
[§] sunando.patra@gmail.com

decays at one loop. Most of the inputs used to extract the Wolfenstein parameters and the related CKM elements are those coming from semileptonic and leptonic decays. At the moment, very precise measurements on the related observables are available which are hence beneficial in constraining the new model parameters contributing to these decays. Here, we analyze the constraints on the new parameters from observables related to the CKM measurements, and comment on the impact of such constraints on DM phenomenology.

The simplest way to devise a dark matter model is by considering a scalar, fermionic, or vector field obeying the SM gauge symmetries whose stability can be ensured by an additional discrete $\mathcal{Z}_2$ symmetry under which the DM is odd but all other SM particles are even. However, in order to annihilate into SM particles and give rise to the correct relic abundance, there has to be a mediator between the dark and visible sectors. The interactions of the mediator with the visible sector may include a nonzero vertex with the SM quark fields among others such that the DM can scatter off a fixed target nuclei and be detected from any hint of nuclear recoil. However, such interactions might also impact important flavor physics observables, which most of the dark matter analyses do not take into consideration. In this paper, we investigate the constraints on the dark matter parameter space from flavor data in the context of a simple dark matter model.

## II. SIMPLIFIED MODEL: FERMION DARK MATTER WITH SPIN-0 MEDIATOR

It is common to use effective field theory to describe the low-energy effects of high-scale NP, in which nonrenormalizable effective operators are added to the SM Lagrangian. However, due to the large energies accessible at the LHC, the interpretation of measurements using an effective theory approach may become questionable under certain circumstances. Therefore, the simplified model approaches [1–6], which often contain both dark matter and mediator particles, have gained more relevance in the collider searches. In those models, the mediator provides the link between the visible SM particles and dark matter. By construction, these simplified models do not contain all of the ingredients present in a UV-complete model of dark matter. However, this approach helps characterize the dark matter production processes in UV-complete models without specifying the entire UV completion. There are different varieties of UV-complete models available in the literature, and it is not feasible to study all of them independently and constrain the parameter spaces. Also, the structures of such models are so rich that it is impossible to determine the underlying new dynamics unambiguously from a limited amount of data. Hence, to constrain the NP parameters from the CKM measurements in this paper, we consider a simplified model with a spin-0 mediator. A similar study for a simplified model with a vector mediator has been left for future work.

As an illustration of our main objective, here we consider an extension of the SM by a singlet Dirac fermion dark matter $\chi$ and a spin-0 particle $S$. The DM decay is stabilized by imposing a discrete $\mathcal{Z}_2$ symmetry under which $\chi \to -\chi$, while all other particles remain even under the transformation. The most general renormalizable Lagrangian for such a model can be written as

$$\begin{aligned}\mathcal{L} = \mathcal{L}_{\rm SM} + \frac{1}{2}\bar{\chi}(i\partial\!\!\!/ - m_\chi)\chi - \frac{1}{2}(\partial_\mu S)^2 \\ - [\bar{\chi}(g'_s + i g'_p\gamma_5)\chi + \bar{\psi}(g_s + i g_p\gamma_5)\psi]S - V(H,S),\end{aligned} \tag{1}$$

where $H$ denotes the SM Higgs doublet and $\psi$ denotes SM fermions. The scalar potential $V(H,S)$ can be of the form

$$\begin{aligned}V(H,S) = \mu_H^2 H^\dagger H + \frac{1}{2}\lambda_H (H^\dagger H)^2 + \mu_1^3 S + \frac{\mu_S^2}{2}S^2 + \frac{\mu_3}{3!}S^3 \\ + \frac{\lambda_S}{4!}S^4 + \lambda_1 (H^\dagger H)S + \frac{\lambda_2}{2}(H^\dagger H)S^2.\end{aligned} \tag{2}$$

For studies based on such models in the literature, see Refs. [7–12]. Also, in our study we mostly focus on effective DM interactions with SM quarks, i.e., $\psi \equiv q$. There are plenty of analyses on such leptophobic DM models from the perspective of LHC and indirect detection searches [2,10–14].

Note that we do not attempt to construct a UV-complete model and constrain the interactions of the mediator with the DM and SM fermions only by the requirement of Lorentz invariance. In Eq. (1), the mediator interaction with the SM fermions is renormalizable. However, it is not invariant under the SM gauge group. Hence, it is expected that the model will break down at a high energy scale $\Lambda$. One can assume that the origin of these interactions is some higher-dimensional nonrenormalizable operator suppressed by the power in $\Lambda$, which is invariant under the SM gauge group. The effective interaction mentioned above could also be generated from a UV complete model via the loop diagrams involving the heavy vector-like fermions that mix with the SM fermions; see, for example, Ref. [15]. There could be other ways as well; however, we have mentioned earlier that we are mostly interested in constraining the new couplings and not in the exact details of the origin of such interactions. Also, we should mention that for a UV-complete description, one may need to add new states and interactions at the energy scale $\Lambda$. We will continue this discussion in the following section.

In this analysis, we consider only quarks and assume universal coupling for all of the quarks for the mediator interaction with the fermions. However, the above Lagrangian can produce large flavor-violating effects due to the coupling of the mediator with SM quarks.

Hence, invoking the prescription of minimal flavor violation, we scale the scalar and pseudoscalar couplings with the SM Yukawa couplings $y_{ij}$ as

$$\mathcal{L}^q_{\rm int} = \sum_{i,j} \bar{q}_i \frac{y^q_{ij}}{\sqrt{2}} (g_s + i g_p \gamma_5) q_j S, \tag{3}$$

where the sum runs over all quark flavors. In order to avoid FCNC, all flavor off-diagonal couplings are set to zero and the diagonal Yukawa couplings are given by $y^q_{ii} = \sqrt{2} m^q_f / v$, where $v = 246$ GeV, is the vacuum expectation value of the Higgs boson. Therefore, Eq. (3) can be simplified as

$$\mathcal{L}^q_{\rm int} = \bar{q}_i \frac{m_{q_i}}{v} (g_s + i g_p \gamma_5) q_i S \tag{4}$$

$$= m_{q_i} \bar{q}_i (C_s + i C_p \gamma_5) q_i S, \tag{5}$$

with $C_s = \frac{g_s}{v}$ and $C_p = \frac{g_p}{v}$. Even though these couplings do not induce FCNCs at tree level, one can have flavor-changing decays of $K$ and $B$ mesons induced by one-loop corrections leading to $s \to dS$ and $b \to d(s)S$ transitions. Constraints on the couplings in Eq. (1) from such decays have been studied in Ref. [16] for mediators of mass $M_S \lesssim 10$ GeV.

Following the Lagrangian given in Eq. (1), it is evident that the dominant channel for DM annihilation will be the $s$-channel transition $\bar{\chi}\chi \to \bar{\psi}\psi$ shown by the Feynman diagram on the lhs of Fig. 1. There can also be a $t$-channel annihilation $\bar{\chi}\chi \to SS$ as shown in Fig. 1 but for heavy scalars, but this contribution will be rather suppressed. The thermally averaged dark matter annihilation cross section $\langle \sigma v \rangle$ is usually expressed as a partial-wave expansion in powers of the square of the relative velocity between the annihilating particles as

$$\langle \sigma v \rangle = a + b \langle v^2 \rangle + d \langle v^4 \rangle + \cdots, \tag{6}$$

where $a$, $b$, $d$ are the leading $s$-wave, $p$-wave, and $d$-wave contributions to the cross section, respectively. The dominant contribution to the $s$-channel DM annihilation rate for pure scalar interaction mediation is velocity suppressed due to the absence of $s$-wave terms. However, in the presence of the pseudoscalar coupling $g'_p$, there is an enhancement in the annihilation cross section due to the presence of an unsuppressed $s$-wave [17]. Also, there will be contributions to the direct-detection (DD) cross section. The advantage of nonzero pseudoscalar interaction is that the weakly interacting massive particle (WIMP)-nucleon scattering cross sections from such operators are spin dependent and velocity suppressed. These kinds of pseudoscalar interactions help to evade stringent bounds from present DD experimental searches. The phenomenology of such pseudoscalar mediators have been extensively studied in Refs. [11,16,18–20]. While the pseudoscalar operators help weaken the DD scattering cross section with a momentum suppression, they also amplify the chances of probing the WIMP at indirect-detection experiments through initial-/final-state radiation or bremsstrahlung processes [21–26]. On the other hand, the only way to obtain a spin-independent DD cross section is to have a nonzero scalar-scalar effective interaction, i.e., $C_s, g'_s \neq 0$.

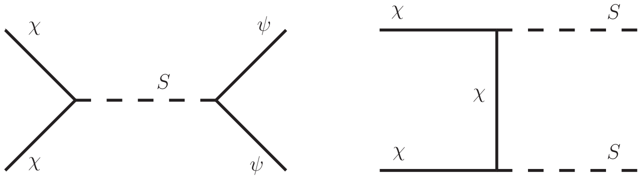

FIG. 1. Annihilation channels for the spin-0-mediated fermionic dark matter model under consideration.

## III. CONTRIBUTIONS IN $d_i \to u_j \ell \nu_\ell$ DECAYS

In the SM, the $d_i \to u_j \ell \nu_\ell$ transitions are tree-level processes mediated by the $W$ boson. Therefore, the $d_i \to u_j W$ vertex has a $V - A$ structure, i.e., $\gamma^\mu (1 - \gamma_5)$. In the previous section, in Eq. (5) we defined a Lagrangian that contains interactions of SM fermions with the scalar $S$. Note that this type of interaction will affect the SM charged-current vertex $\bar{d}_j \gamma^\mu (1 - \gamma_5) u_i W_\mu$ at one loop, resulting in new contributions in the semileptonic or purely leptonic decay rates $\Gamma_{(d_j \to u_i \ell \nu_\ell)}$ ($\ell =$ leptons). A representative diagram is shown in Fig. 2, wherein these decays receive vertex corrections from the heavy scalar exchanges in the loop. The CKM element $V_{ij}$ appears as a vertex factor of the charged-current interactions in the SM. As will be shown in the next subsection, the corrections due to NP have a direct impact on the vertex factors, which in this case are the CKM elements multiplied by the $SU(2)_L$ gauge coupling: $V_{ij} \frac{g}{\sqrt{2}}$. The vertex correction shown in Fig. 2 may introduce additional operators other than $(V - A)$ type.

The most general effective Hamiltonian for the $d_i \to u_j \ell \nu$ processes can be expressed as [27,28]

$$\mathcal{H}^{d_i \to u_j}_{\rm eff} = \frac{4 G_F}{\sqrt{2}} V_{ij} [(\delta_{\ell\ell} + C^\ell_{V_1}) \mathcal{O}^\ell_{V_1} + C^\ell_{V_2} \mathcal{O}^\ell_{V_2} + C^\ell_{S_1} \mathcal{O}^\ell_{S_1} + C^\ell_{S_2} \mathcal{O}^\ell_{S_2} + C^\ell_T \mathcal{O}^\ell_T], \tag{7}$$

where $C^\ell_X$ ($X = V_1, V_2, S_1, S_2, T$) are the Wilson coefficients (WCs) corresponding to the operator basis

$$\begin{aligned}
\mathcal{O}^\ell_{V_1} &= (\bar{u}_{jL} \gamma^\mu d_{iL})(\bar{\ell}_L \gamma_\mu \nu_L), \\
\mathcal{O}^\ell_{V_2} &= (\bar{u}_{jR} \gamma^\mu d_{iR})(\bar{\ell}_L \gamma_\mu \nu_L), \\
\mathcal{O}^\ell_{S_1} &= (\bar{u}_{jL} d_{iR})(\bar{\ell}_R \nu_L), \\
\mathcal{O}^\ell_{S_2} &= (\bar{u}_{jR} d_{iL})(\bar{\ell}_R \nu_L), \\
\mathcal{O}^\ell_T &= (\bar{u}_{jR} \sigma^{\mu\nu} d_{iL})(\bar{\ell}_R \sigma_{\mu\nu} \nu_L).
\end{aligned} \tag{8}$$

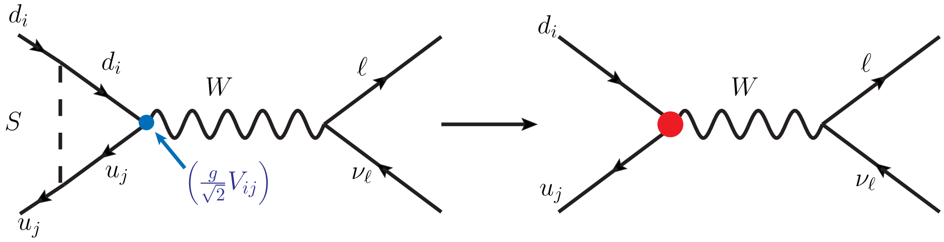

FIG. 2. Loop correction to the $d_i \to u_j W$ vertex in the presence of a real scalar $S$. The vertex modification will have direct impact on the vertex CKM factor $V_{ij}$.

There are no lepton-flavor-violating vertices in the Lagrangian (5). Hence, for all practical purposes, we can remove the suffix $\ell$ in the operator basis and write $C_X^\ell \equiv C_X$. Note that in the SM, only $\mathcal{O}_{V_1}$ contributes at the tree level. Along with $\mathcal{O}_{V_1}$, the rest of the operators may appear by themselves or as combinations in different NP scenarios. The WC $C_X$ incorporates the NP effects in these decays, and therefore in the SM, $C_X = 0$.

The detailed mathematical expressions of the decay rate distributions for the exclusive semileptonic ($P \to M^{(*)}\ell\nu_\ell$) and purely leptonic ($P \to \ell\nu_\ell$) decays can be found in Ref. [27], where $P$ and $M$ are the pseudoscalar mesons and $M^*$ is a vector meson. The semileptonic and purely leptonic decay rates are directly proportional to the vertex factors. Here, we would like to mention that most of the CKM elements, like $|V_{ud}|$, $|V_{cd}|$, $|V_{us}|$, $|V_{cs}|$, $|V_{ub}|$, and $|V_{cb}|$, are extracted from the semileptonic and purely leptonic (in some cases) $d_i \to u_j\ell\nu_\ell$ decays, with $\ell = \mu$, or $e$. The underlying assumption is that these decays with the light leptons will be less sensitive to any NP effect. The measured decay rates, along with some other inputs from lattice calculations (decay constants and form factors), are useful probes for the CKM elements $|V_{ij}|$. In the presence of new four-fermion operators in accordance with Eq. (7), the decay rates will be modified. If only the vertex factor is modified, then the extracted values of the $|V_{ij}|$ can be directly used to constrain the new couplings; otherwise, we need to fit the decay rates themselves. In the following subsections, we will discuss this in detail.

Also, it is important to mention that all of these CKM elements are extracted with reasonably good precision. For example, $|V_{ud}|$ and $|V_{cs}|$ are known with an error ≈0.01%, while $|V_{us}|$ and $|V_{cd}|$ are known with an accuracy of 0.1%. $|V_{ub}|$ and $|V_{cb}|$ are relatively less precisely known. Therefore, it is natural to expect tight constraints on the new couplings $C_s$ and $C_p$ from an analysis of the CKM observables, and purely leptonic and semileptonic decay rates, respectively. Note that $|V_{ub}|$ and $|V_{cb}|$ are also extracted from semileptonic inclusive decays. We do not consider the inputs from inclusive decays to constrain the new couplings. The extraction of $|V_{cb}|$ from the inclusive decays requires a complex fit to the respective decay rates and moments. Considering leading-order power corrections up to order $1/m_b^5$, one needs to fit 18 nonperturbative matrix elements alongside $|V_{cb}|$, $m_b$, and $m_c$ [29–31]. Due to the insufficient number of inputs, model assumptions are used in the fit for a couple of higher-order nonperturbative matrix elements. On top of this, unknown higher-order corrections to the nonperturbative matrix elements are also relevant to improve the precision of $|V_{cb}|$, which may be small compared to the known ones but are missing at the moment. The study of NP contributions in the inclusive decays is a dedicated project where we need to analytically calculate the NP contributions in the decay rates, as well as in the hadronic, leptonic, and $q^2$ moments, and then one needs to do a simultaneous fit. Here, the dependencies of these observables on the new physics parameters will not be simple. Hence, extractions of new physics information will not be very clean. The situation is even worse in the inclusive determination of $|V_{ub}|$. Here, the results are completely dependent on the QCD modeling of the non-perturbative shape functions on top of the nonperturbative matrix elements. There are four different methods used in the literature to model the shape function, and the extracted values of $|V_{ub}|$ in each of these methods do not exactly agree with each other [28,32]. Therefore, it is natural to expect that before constraining NP from inclusive $b \to u\ell\nu_\ell$, we first need to understand the underlying methodology.

On the contrary, we have a sufficient number of inputs from experiments and lattice calculations for the exclusive determinations $|V_{ub}|$ and $|V_{cb}|$. Note that the respective rates have a very simple dependence on the new Wilson coefficients in these decays. Hence, the extractions of these coefficients will be relatively clean compared to that from the inclusive decays, given the complexity of the fit in the inclusive decays, as discussed above. Numerically, we do not expect any changes in the allowed parameter spaces of new coefficients from the inclusive of inclusive decays. Also, it should be noted that the majority of the other inputs used in the CKM fit analysis have relatively better precision than $|V_{ub}|$ and $|V_{cb}|$ from inclusive decays.

### A. Effective vertex

As mentioned earlier, in the SM the coupling strength for the $d_i \to u_j W$ charged-current interaction is given by $\frac{igV_{ij}}{\sqrt{2}}$

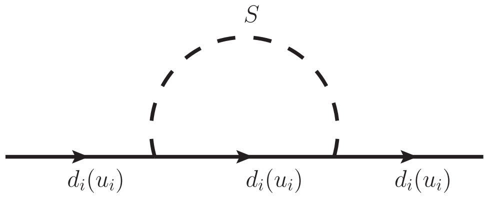

FIG. 3. Quark self-energy corrections in the presence of the new interaction given in Eq. (5).

and the interaction is of the type $(V-A)$. However, the one-loop correction of this charged-current vertex due to the interaction given in Eq. (5) introduces one new $(V+A)$-type interaction in addition to the original $(V-A)$-type interaction. The corresponding Feynman diagram can be seen in Fig. 2, and the effective charged-current interaction can be written as

$$\begin{aligned}\mathcal{L}^{\mathrm{eff}}_{d_i\to u_j W} &= \frac{igV_{ij}}{2\sqrt{2}}[C_L\bar{u}_j\gamma_\mu(1-\gamma_5)d_i + C_R\bar{u}_j\gamma_\mu(1+\gamma_5)d_i]W^\mu \\ &= \frac{igV_{ij}}{2\sqrt{2}}[C_L\mathcal{O}_L + C_R\mathcal{O}_R]W^\mu. \qquad (9)\end{aligned}$$

Here, the effects of NP coming from the loop corrections are introduced in the coefficients $C_L$ and $C_R$. Hence, we can say that at the tree level (pure SM) $C_L = 1$ and $C_R = 0$. We perform the calculation in a unitary gauge using dimensional regularization and find that the one-loop contribution to the charged-current vertex is in general divergent. The loop factor $C_L$ does not receive any $\frac{1}{\epsilon}$ pole from Fig. 2; however, $C_R$ has a pole. Note that there will be a contribution to $C_L$ from the vertex counterterm. The relevant part of the counterterm can be obtained from the wave-function renormalization which we calculate from the quark self-energy correction diagram given in Fig. 3. For the renormalization we follow the $\overline{\mathrm{MS}}$ scheme.

Note that the overall contributions in $C_L$ and $C_R$ will be divergent, and we do not have any additional contributions to remove these divergences. It is well known that in simplified models such as those defined above, the one-loop contributions to flavor-changing transitions are in general UV divergent; see, for example, Refs. [17,33,34]. To make the theory renormalizable, one may need to add new states with tree-level charged-current interactions with the SM fermions. However, the available data will constrain such an interaction in general. As mentioned earlier, such divergences reflect the dependence of our results on the suppression scale $\Lambda$ (the scale at which new states might appear). Therefore, we interpret our model as an effective theory below some new physics scale $\Lambda$ with the following replacement: $1/\epsilon + \mathrm{Log}(\mu^2/m^2) \to \mathrm{Log}(\Lambda^2/m^2)$. In a UV-complete theory, the additional NP at the scale $\Lambda$ is expected to cancel the divergences that are present. Here, we take an optimistic view and assume that the new high-scale (higher-dimensional operators) contributions in the low-energy observables will have a negligible impact on our analysis. The renormalization group evolution over the energy range that we consider here will not change the coupling structure significantly.

After obtaining the contributions in $C_L$ and $C_R$ and integrating out the $W$ field from the diagram of Fig. 2, we obtain the following effective Hamiltonian:

$$\mathcal{H}^{d_i\to u_j}_{\mathrm{eff}} = \frac{4G_F}{\sqrt{2}}V_{ij}[(1+C_{V_1})\mathcal{O}_{V_1} + C_{V_2}\mathcal{O}_{V_2}], \qquad (10)$$

where the operators are defined in Eq. (9). The WCs $C_{V_1}$ and $C_{V_2}$ will be obtained from $C_L$ and $C_R$. In the leading-log approximation, the WCs can be expressed as

$$C^{q_i\to q_j}_{V_1} = -\frac{C_T}{64\pi^2}m^2_{q_i}\,\log\frac{\Lambda^2}{m^2_{q_i}}, \qquad (11)$$

$$C^{q_i\to q_j}_{V_2} = -\frac{C_T}{32\pi^2}m_{q_i}m_{q_j}\,\log\frac{\Lambda^2}{m^2_{q_i}}, \qquad (12)$$

where $C_T \equiv (C_s^2 + C_p^2) = (g_s^2 + g_p^2)/v^2$. We have dropped the other finite contributions, which are small effects compared to the one given in the above equations. It is important to note that the loop contribution is zero in the massless quark limit for light quarks, such as $u$, $d$, $s$, etc. In the above we have chosen the scale $\Lambda$ as the UV cutoff, while the IR scales will be decided by the respective decaying quark masses.

We want to point out that in the SM we can have similar vertex corrections with the scalar $S$ replaced by the SM Higgs or by a $Z$ boson in Fig. 2. We can parametrize such corrections as $\delta C^{\mathrm{SM}}_{V_1}$, which represents a small shift from $C^{\mathrm{SM}}_{V_1} = 1$. For SM Higgs, there will not be any contribution in $C_{V_2}$ and the contribution in $\delta C^{\mathrm{SM}}_{V_1}$ is $\lesssim 10^{-8}$. For the SM $Z$ boson, the contributions to both $\delta C^{\mathrm{SM}}_{V_1}$ and $C_{V_2}$ are negligibly small compared to the new contribution in $C_{V_2}$. We hence drop any such contributions in our analysis since they have a negligible impact on our findings.

### B. Contributions in the decays: Semileptonic and leptonic

Using the effective Hamiltonian given in Eq. (10), the differential decay rate for the $P\to M\ell\nu_\ell$ transition is written as [35]

$$\begin{aligned}&\frac{d\Gamma(P\to M\ell\nu_\ell)}{dq^2} \\ &= \frac{G_F^2|V_{ij}|^2}{\pi^3 m_P^3}q^2\sqrt{\lambda_M(q^2)}\left(1-\frac{m_\ell^2}{q^2}\right)|1+C_{V_1}+C_{V_2}|^2 \\ &\quad\times\left\{\left(1+\frac{m_\ell^2}{2q^2}\right){H^s_{V,0}}^2 + \frac{3}{2}\frac{m_\ell^2}{q^2}{H^s_{V,t}}^2\right\}, \qquad (13)\end{aligned}$$

while that for $P \to M^* \ell \nu_\ell$ is

$$\frac{d\Gamma(P \to M^* \ell \nu_\ell)}{dq^2} = \frac{G_F^2 |V_{ij}|^2}{\pi^3 m_P^3} q^2 \sqrt{\lambda_{M^*}(q^2)} \left(1 - \frac{m_\ell^2}{q^2}\right) \times \left\{ (|1 + C_{V_1}|^2 + |C_{V_2}|^2) \left[ \left(1 + \frac{m_\ell^2}{2q^2}\right)(H_{V,+}^2 + H_{V,-}^2 + H_{V,0}^2) + \frac{3}{2}\frac{m_\ell^2}{q^2} H_{V,t}^2 \right] - 2\mathcal{R}e[(1 + C_{V_1})C_{V_2}^*] \left[ \left(1 + \frac{m_\ell^2}{2q^2}\right)(H_{V,0}^2 + 2H_{V,+}H_{V,-}) + \frac{3}{2}\frac{m_\ell^2}{q^2} H_{V,t}^2 \right] \right\}. \tag{14}$$

The helicity amplitudes are written in terms of the QCD form factors as

$$H_{V,0}^s(q^2) = \sqrt{\frac{\lambda_M(q^2)}{q^2}} f_+(q^2), \tag{15a}$$

$$H_{V,t}^s(q^2) = \frac{m_P^2 - m_M^2}{\sqrt{q^2}} f_0(q^2), \tag{15b}$$

and

$$H_{V,\pm}(q^2) = (m_P + m_{M^*}) A_1(q^2) \mp \frac{\sqrt{\lambda_{M^*}(q^2)}}{m_P + m_{M^*}} V(q^2), \tag{16a}$$

$$H_{V,0}(q^2) = \frac{m_P + m_{M^*}}{2 m_{M^*} \sqrt{q^2}} \left[ -(m_P^2 - m_{M^*}{}^2 - q^2) A_1(q^2) + \frac{\lambda_{M^*}(q^2)}{(m_P + m_{M^*})^2} A_2(q^2) \right], \tag{16b}$$

$$H_{V,t}(q^2) = -\sqrt{\frac{\lambda_{M^*}(q^2)}{q^2}} A_0(q^2). \tag{16c}$$

The branching fraction for $P \to \ell \nu_\ell$ corresponding to the same Hamiltonian is

$$\mathcal{B}(P \to \ell \nu_\ell) = \frac{\tau_P}{8\pi} m_P m_\ell^2 f_P^2 G_F^2 \left(1 - \frac{m_\ell^2}{m_P^2}\right)^2 \times |V_{ij}(1 + C_{V_1} - C_{V_2})|^2. \tag{17}$$

From the above decay rate distributions, we can see that the new contributions to $P \to M \ell \nu_\ell$ and $P \to \ell \nu_\ell$ decays will modify only the vertex from $|V_{ij}| \to |V'_{ij}| = |V_{ij}(1 + C_{V_1} \pm C_{V_2})|$. However, in $P \to M^* \ell \nu_\ell$ transitions the new contributions will modify the $q^2$ distribution. Therefore, the CKM elements $|V'_{ij}|$ extracted from purely leptonic or $P \to M \ell \nu_\ell$ decays can be directly used to constrain the new parameters along with the Wolfenstein parameters ($A$, $\lambda$, $\rho$, and $\eta$) with which we need to parametrize $|V_{ij}|$. Note that $|V_{cb}|$ is extracted from both $B \to D \ell \nu_\ell$ and $B \to D^* \ell \nu_\ell$ decays. Hence, to extract the Wolfenstein parameters along with the new parameters from $B \to D^* \ell \nu_\ell$ decays, we need to redo the fit to the experimental data. We discuss the relevant details in the next section.

## IV. NUMERICAL ANALYSIS AND RESULTS

### A. $B \to D^* \ell \nu$ observables

As pointed out in the previous section, for the NP scenario under consideration we need to fit the decay rate distributions of $B \to D^* \ell \nu_\ell$ decays to extract the CKM parameters along with the NP parameters. The methodology of this fit will be similar to the one given in Refs. [36,37] with very recent updates from the Fermilab Lattice Collaboration [38]. For the first time, they have provided the $B \to D^*$ form factors at nonzero recoil. They provided a set of synthetic data based on the Boyd-Grinstein-Lebed (BGL) parametrization [39] of the form factors truncated at $N = 2$ at three $w$ values, $\{1.03, 1.10, 1.17\}$, along with their correlations. We use these data points in our analysis. In accordance with our previous work, we utilize the untagged data set for the fourfold decay distribution corresponding to $B \to D^* \ell \nu$ by the Belle Collaboration [40]. We also use the $B \to D^*$ form factors at $q^2 = 0$ from QCD light-cone sum rules (LCSR) [41]. Additionally, the Fermilab/MILC lattice input, $h_{A_1}(1) = 0.906(13)$ [42], allows us to efficiently constrain the form factor parameter $a_0^f$, and hence $|V_{cb}|$. In our analysis we do not consider the data set of unfolded differential decay rates of four kinematic variables for $\bar{B}^0 \to D^{*+} \ell^- \bar{\nu}_\ell$ provided by Belle in 2017 [43] since the data remains unpublished to date. However, in Appendix C we provide our fit results by including this data set. As we will see later, the inclusion of this data does not affect our fit results much.

The four form factors relevant for $B \to D^* \ell \nu_\ell$ decays are $\mathcal{F}_i = \{f(z), g(z), \mathcal{F}_1(z), \mathcal{F}_2(z)\}$. In the BGL method of parametrization, these form factors can be expressed as a series expansion in $z$ as

$$\mathcal{F}_i(z) = \frac{1}{P_i(z)\phi_i(z)} \sum_{j=0}^{N} a_j^{\mathcal{F}_i} z^j, \tag{18}$$

TABLE I. Fit result for the frequentist analysis of the mentioned $B \to D^* \ell \bar{\nu}_\ell$ data set for the SM scenario.

| | Fit quality | | | |
|---|---|---|---|---|
| Data set | $\chi^2$/d.o.f. | $p$-value | Parameter | Fit result |
| Belle 2018 [40] + $h_{A_1}(1)$ [42] + LCSR [41] + lattice [38] | 52.82/45 | 19.75% | $\lvert V_{cb} \rvert$ | $38.69(79) \times 10^{-3}$ |
| | | | $a_0^f$ | 0.0123(1) |
| | | | $a_1^f$ | 0.0222(96) |
| | | | $a_2^f$ | −0.522(196) |
| | | | $a_0^g$ | 0.0318(10) |
| | | | $a_1^g$ | −0.133(63) |
| | | | $a_2^g$ | −0.62(146) |
| | | | $a_1^{\mathcal{F}_1}$ | 0.0021(15) |
| | | | $a_0^{\mathcal{F}_2}$ | 0.0515(12) |
| | | | $a_1^{\mathcal{F}_2}$ | −0.149(59) |
| | | | $a_2^{\mathcal{F}_2}$ | 0.987(932) |

where $z$ is related to the recoil angle $w$ as

$$z = \frac{\sqrt{w+1} - \sqrt{2}}{\sqrt{w+1} + \sqrt{2}}. \tag{19}$$

The recoil angle is related to the momentum transfer $q^2$ as $q^2 = m_B^2 + m_{D^*}^2 - 2 m_B m_{D^*} w$. The functions $P_i(z)$, called the Blaschke factors, are given by

$$P_i(z) = \prod_p \frac{z - z_p}{1 - z z_p}, \tag{20}$$

which are used to eliminate the poles at $z = z_p$, where

$$z_p = \frac{\sqrt{(m_B + m_{D^*})^2 - m_P^2} - \sqrt{4 m_B m_{D^*}}}{\sqrt{(m_B + m_{D^*})^2 - m_P^2} + \sqrt{4 m_B m_{D^*}}}. \tag{21}$$

Here $m_P$ denotes the pole masses and can be found in Ref. [44]. The outer functions $\phi_i(z)$ are chosen to be

$$\begin{aligned}
\phi_f &= \frac{4r}{m_B^2} \sqrt{\frac{n_I}{6\pi \chi_{1^+}^T(0)}} \frac{(1+z)(1-z)^{3/2}}{[(1+r)(1-z) + 2\sqrt{r}(1+z)]^4}, \\
\phi_g &= 16 r^2 \sqrt{\frac{n_I}{3\pi \tilde{\chi}_{1^-}^T(0)}} \frac{(1+z)^2(1-z)^{-1/2}}{[(1+r)(1-z) + 2\sqrt{r}(1+z)]^4}, \\
\phi_{\mathcal{F}_1} &= \frac{4r}{m_B^3} \sqrt{\frac{n_I}{6\pi \chi_{1^+}^T(0)}} \frac{(1+z)(1-z)^{5/2}}{[(1+r)(1-z) + 2\sqrt{r}(1+z)]^5}, \\
\phi_{\mathcal{F}_2} &= 8\sqrt{2} r^2 \sqrt{\frac{n_I}{\pi \tilde{\chi}_{1^+}^L(0)}} \frac{(1+z)^2(1-z)^{-1/2}}{[(1+r)(1-z) + 2\sqrt{r}(1+z)]^4},
\end{aligned} \tag{22}$$

where $r = m_{D^*}/m_B$ and the other inputs can be found in Ref. [44]. Therefore, for $N = 2$, there are 12 coefficients $a_j^{\mathcal{F}_i}$ for the four form factors. These coefficients satisfy the following weak unitarity constraints:

$$\sum_{j=0}^{N} (a_j^g)^2 < 1, \quad \sum_{j=0}^{N} (a_j^f)^2 + (a_j^{\mathcal{F}_1})^2 < 1, \quad \sum_{j=0}^{N} (a_j^{\mathcal{F}_2})^2 < 1. \tag{23}$$

Furthermore, there are two kinematical constraints on the form factors, one each at zero and maximum recoil:

$$\mathcal{F}_1(1) = m_B(1-r) f(1), \tag{24}$$

$$\mathcal{F}_2(w_{\max}) = \frac{1+r}{m_B^2 (1 + w_{\max})(1-r) r} \mathcal{F}_1(w_{\max}). \tag{25}$$

We consider these constraints in our analysis to remove two of the BGL coefficients from the theory. In the limit of massless leptons, the decay distribution becomes insensitive to the form factor $\mathcal{F}_2$. Hence, only eight independent form factor coefficients are required to fit the theory to the data. For the numerical analysis presented here, we perform a maximum likelihood estimation of the parameters using Optex, a *Mathematica*-based package. The fit results are provided in Table I. The value of $\lvert V_{cb} \rvert$ is extremely consistent with the one obtained in Ref. [38].[1] In the following section we utilize this value of $\lvert V_{cb} \rvert$ for a global CKM fit without NP.

## B. CKM fit

As we mentioned in the previous section, the NP contributions to semileptonic ($P \to M \ell \nu_\ell$) and leptonic decays will impact the vertex factor, which is proportional to the square of the magnitude of the corresponding CKM element. Hence, we need to extract the parameters related to NP alongside the other Wolfenstein parameters.

---

[1] In Table XV in Appendix C, we check the fit by additionally including the 2017 Belle data. We find that the value of $\lvert V_{cb} \rvert$ is consistent with the value obtained without this data set at $1\sigma$ C.L.

TABLE II. Comparison of the best-fit estimates of the Wolfenstein parameters by the CKMFitter group and our group from the global CKM fit in the SM framework. The two results are consistent with each other at $1\sigma$. We also provide the $\chi^2/\text{d.o.f.}$ and the goodness of fit for our fit results. The last row contains the best parameter estimates of the global scenario with the most updated inputs.

| | | | | | Fit quality | |
|---|---|---|---|---|---|---|
| | $A$ | $\lambda$ | $\bar{\rho}$ | $\bar{\eta}$ | $\chi^2/\text{d.o.f.}$ | $p$-value |
| CKMFitter 2019 | $0.8235^{+0.0056}_{-0.0145}$ | $0.224837^{+0.000251}_{-0.000060}$ | $0.1569^{+0.0102}_{-0.0061}$ | $0.3499^{+0.0079}_{-0.0065}$ | ... | ... |
| Our result | $0.8205 \pm 0.0075$ | $0.22462 \pm 0.00031$ | $0.1607 \pm 0.0093$ | $0.3558 \pm 0.0088$ | 34.18/23 | 6.26% |
| Updated 2021 results | $0.8178 \pm 0.0070$ | $0.22498 \pm 0.00029$ | $0.1734 \pm 0.0092$ | $0.374 \pm 0.011$ | 37.25/25 | 8.37% |

This means that we need to carry out a dedicated fit to all of these parameters using the machinery used by the CKMFitter group to fit only the CKM parameters.

To validate the code, we recreate the "Summer'19" SM fit performed by the CKMFitter group using the same set of inputs and observables as mentioned in Ref. [45]. The details of the theoretical expressions for the observables can be found in Refs. [27,46–48]. We report our fit results in Table II and compare them to the CKMFitter 2019 results. They are consistent with each other at $1\sigma$ C.L. We go a step

TABLE III. List of observables used for the CKM fit (*Updated 2021*) in the SM framework. For the NP analysis we have not used the inclusive measurements of $|V_{ub}|$ and $|V_{cb}|$. All other inputs have been considered. Additionally, we have also considered the anomalous $Wtb$ couplings as listed in the last two rows.

| Observable | Value | Reference |
|---|---|---|
| $\lvert V_{ud}\rvert$ (nucl) | $0.97420 \pm 0.00021$ | [49] |
| $\lvert V_{us}\rvert f_+^{K\to\pi}(0)$ | $0.2165 \pm 0.0004$ | [50] |
| $\lvert V_{cd}\rvert_{\nu N}$ | $0.30 \pm 0.011$ | [28] |
| $\lvert V_{cs}\rvert_{W\to c\bar{s}}$ | $0.94^{+0.32}_{-0.26} \pm 0.13$ | [28] |
| $\lvert V_{ub}\rvert_{\text{excl}}$ | $(3.91 \pm 0.13) \times 10^{-3}$ | [51,52] |
| $\lvert V_{ub}\rvert_{\text{incl}}$ | $(4.10^{+0.09}_{-0.22} \pm 0.15) \times 10^{-3}$ | [53] |
| $\lvert V_{cb}\rvert_{B\to D}$ | $(40.84 \pm 1.15) \times 10^{-3}$ | [36] |
| $\lvert V_{cb}\rvert_{B\to D^*}$ | $(38.69 \pm 0.79) \times 10^{-3}$ | This work |
| $\lvert V_{cb}\rvert_{\text{incl}}$ | $(42.16 \pm 0.50) \times 10^{-3}$ | [54] |
| $\mathcal{B}(\Lambda_p \to p\mu^-\bar{\nu}_\mu)_{q^2>15}/\mathcal{B}(\Lambda_p \to \Lambda_c\mu^-\bar{\nu}_\mu)_{q^2>7}$ | $(0.947 \pm 0.081) \times 10^{-2}$ | [55] |
| $\mathcal{B}(B^- \to \tau^-\bar{\nu}_\tau)$ | $(1.09 \pm 0.24) \times 10^{-4}$ | [27] |
| $\mathcal{B}(D_s^- \to \mu^-\bar{\nu}_\mu)$ | $(5.51 \pm 0.16) \times 10^{-3}$ | [27] |
| $\mathcal{B}(D_s^- \to \tau^-\bar{\nu}_\tau)$ | $(5.52 \pm 0.24) \times 10^{-2}$ | [27] |
| $\mathcal{B}(D^- \to \mu^-\bar{\nu}_\mu)$ | $(3.77 \pm 0.18) \times 10^{-4}$ | [27] |
| $\mathcal{B}(D^- \to \tau^-\bar{\nu}_\tau)$ | $(1.20 \pm 0.27) \times 10^{-3}$ | [27] |
| $\mathcal{B}(K^- \to e^-\bar{\nu}_e)$ | $(1.582 \pm 0.007) \times 10^{-5}$ | [28] |
| $\mathcal{B}(K^- \to \mu^-\bar{\nu}_\mu)$ | $0.6356 \pm 0.0011$ | [28] |
| $\mathcal{B}(\tau^- \to K^-\bar{\nu}_\tau)$ | $(0.6986 \pm 0.0085) \times 10^{-2}$ | [27] |
| $\mathcal{B}(K^- \to \mu^-\bar{\nu}_\mu)/\mathcal{B}(\pi^- \to \mu^-\bar{\nu}_\mu)$ | $1.3367 \pm 0.0029$ | [28] |
| $\mathcal{B}(\tau^- \to K^-\bar{\nu}_\tau)/\mathcal{B}(\tau^- \to \pi^-\bar{\nu}_\tau)$ | $(6.438 \pm 0.094) \times 10^{-2}$ | [27] |
| $\mathcal{B}(B_s \to \mu^+\mu^-)$ | $(2.9 \pm 0.7 \pm 0.2) \times 10^{-9}$ | [56] |
| $\lvert V_{cd}\rvert f_+^{D\to\pi}(0)$ | $0.1426 \pm 0.0018$ | [27] |
| $\lvert V_{cs}\rvert f_+^{D\to K}(0)$ | $0.7180 \pm 0.0033$ | [27] |
| $\lvert \varepsilon_K\rvert$ | $(2.228 \pm 0.011) \times 10^{-3}$ | [28] |
| $\Delta m_d$ | $(0.5065 \pm 0.0019)\ \text{ps}^{-1}$ | [27] |
| $\Delta m_s$ | $(17.757 \pm 0.021)\ \text{ps}^{-1}$ | [27] |
| $\sin 2\beta$ | $0.71 \pm 0.09$ | [27] |
| $\phi_s$ | $-0.055 \pm 0.021$ | [27] |
| $\alpha$ | $(85.2^{+4.8}_{-4.3})^\circ$ | [27] |
| $\gamma$ | $(67 \pm 4)^\circ$ | [57] |
| $V_L$ | $0.995 \pm 0.021$ | [28] |
| $V_R$ | $[-0.11, 0.16]$ | [58] |

TABLE IV. List of additional inputs for the CKM fit.

| Input parameters | Value | Reference |
|---|---|---|
| $f_+^{K\to\pi}(0)$ | 0.9706(27) | $N_f = 2+1+1$ [59] |
| $f_{K^\pm}/f_{\pi^\pm}$ | 1.1932(19) | $N_f = 2+1+1$ [59] |
| $f_K$ | $155.7 \pm 0.13$ | $N_f = 2+1+1$ [59] |
| $f_+^{DK}(0)$ | 0.747(19) | $N_f = 2+1+1$ [59] |
| $f_+^{D\pi}(0)$ | 0.666(29) | $N_f = 2+1$ [59] |
| $f_{B_s}$ | 230.3(1.3) MeV | $N_f = 2+1+1$ [59] |
| $f_{B_s}/f_B$ | 1.209(0.005) | $N_f = 2+1+1$ [59] |
| $B_K$ | 0.7625(97) | $N_f = 2+1$ [59] |
| $f_{D_s}$ | 249.9(5) MeV | $N_f = 2+1+1$ [59] |
| $f_{D_s}/f_D$ | 1.1783(16) | $N_f = 2+1+1$ [59] |
| $\zeta(\Lambda_p \to p\mu^-\bar{\nu}_\mu)_{q^2>15}/\zeta(\Lambda_p \to \Lambda_c\mu^-\bar{\nu}_\mu)_{q^2>7}$ | $1.471 \pm 0.096 \pm 0.290$ | [60] |
| $B_{B_s}$ | $1.327 \pm 0.016 \pm 0.030$ | [59] |
| $B_{B_s}/B_{B_d}$ | $1.007 \pm 0.013 \pm 0.014$ | $N_f = 2$ [59] |
| $\bar{m}_c(m_c)$ | $1.2982 \pm 0.0013 \pm 0.0120$ GeV | [60] |
| $\bar{m}_t(m_t)$ | $(165.26 \pm 0.11 \pm 0.30$ GeV | [60] |
| $\eta_{tt}$ | $0.402 \pm 0 \pm 0.007$ | [60] |
| $\eta_{ut}$ | $0.55 \pm 0 \pm 0.024$ | [60] |
| $\eta_B(\bar{M}S)$ | $0.5510 \pm 0 \pm 0.0022$ | [60] |

further and use some recent updates for the CKM observables as listed in Table III and redo the fit in this "Updated 2021" scenario. These are the most up-to-date global fit results after CKMFitter 2019. The other relevant inputs are provided in Table IV. Note that the fit results for all four parameters are consistent with the 2019 results within $1\sigma$. However, the fit values for $\bar{\rho}$ and $\bar{\eta}$ are slightly higher than earlier. The best-fit points for $\bar{\rho}$ have increased by 8%, while those for $\bar{\eta}$ have increased by about 5%. Primarily, these shifts are due to changes in the inputs of $\alpha$, $\gamma$, and

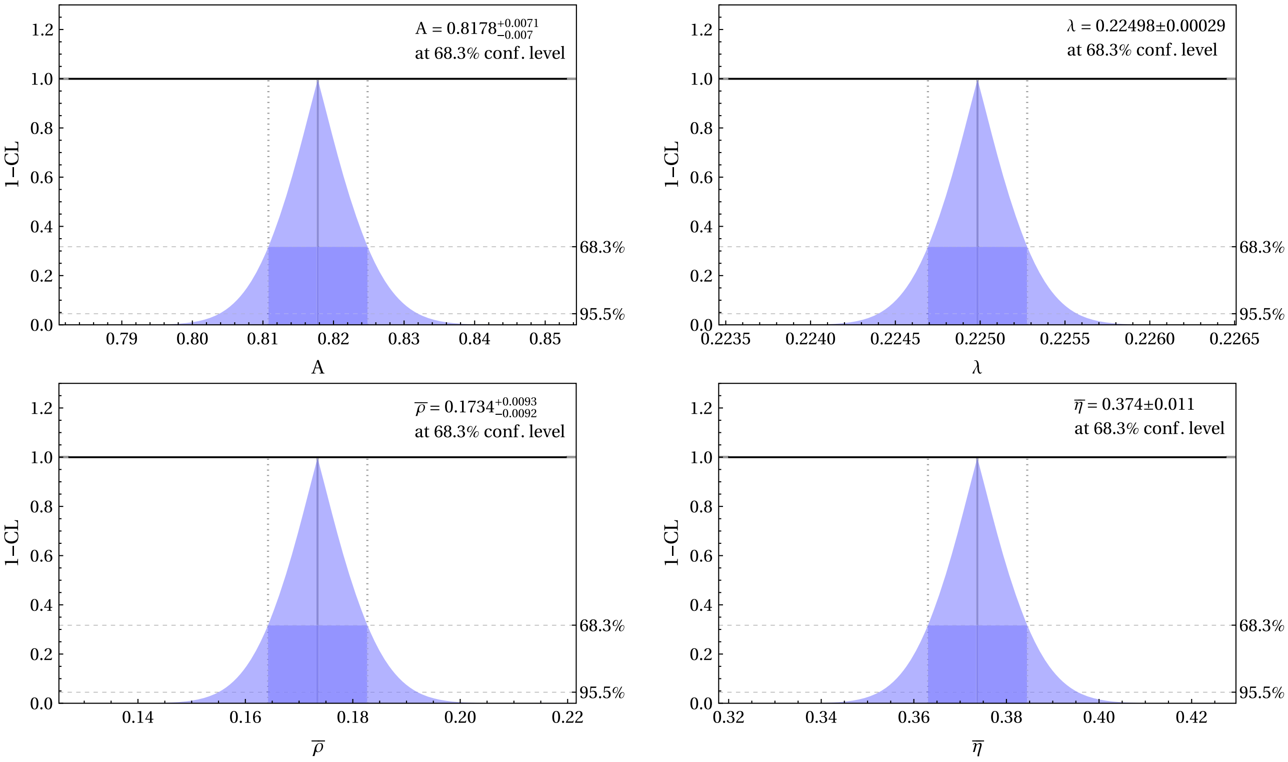

FIG. 4. One-dimensional profile likelihoods for the CKM Wolfenstein parameters $A, \lambda, \bar{\rho}$, and $\bar{\eta}$ for the global CKM 2021 SM fit. The best-fit estimates at 68.3% C.L. are mentioned in each case.

$\sin 2\beta$ which have been updated from the previous 2019 inputs. Figure 4 shows the single-parameter profile likelihoods for the global CKM fit with the most up-to-date inputs and observables. These are the most up-to-date best-fit estimates for the CKM parameters.

### C. CKM fit including new physics

As mentioned earlier, due to the presence of the WC corresponding to the $V+A$ operator $\mathcal{O}_{V_2}$, the decay distribution of $P \to M^* \ell \nu_\ell$ decays will be modified, unlike the alteration of the vertex CKM factor in case of the $P \to M \ell \nu_\ell$ and $P \to \ell \nu_\ell$ decays. Hence, in order to perform the fit for the NP scenarios, we consider both CKM observables listed in Table III as well as the list of $B \to D^* \ell \bar{\nu}_\ell$ data mentioned in the previous subsection. However, we do not consider the inclusive determinations of $|V_{ub}|$ and $|V_{cb}|$ for the NP fit, as mentioned earlier. Additionally, we also consider the $Wtb$ anomalous couplings as observables which are significantly affected by heavy beyond-the-SM physics like the present model. The most general $Wtb$ vertex is expressed as

$$\mathcal{L}_{Wtb} = -\frac{g}{\sqrt{2}} \bar{b} \gamma^\mu (V_L P_L + V_R P_R) t W^- - \frac{g}{\sqrt{2}} \bar{b} \frac{i\sigma^{\mu\nu}}{M_W} (g_L P_L + g_R P_R) t W^- + \mathrm{H.c.} \tag{26}$$

In the SM, $V_L = V_{tb} \simeq 1$ while the other anomalous couplings $V_R$, $g_L$, $g_R$ are equal to zero. Limits have been set on such couplings by analyzing CMS and ATLAS data on helicity fractions, the single top production cross section, and forward-backward asymmetries [58,61,62]. In our model, contributions to these couplings will be much enhanced since they are proportional to the top-quark mass. As listed in Table III, we use them as inputs in our analysis. Note that the NP contribution to the tensor operator $\sigma^{\mu\nu}$ is much suppressed and therefore we do not consider the anomalous couplings $g_L$ and $g_R$ in our analysis.

To begin with, we present the fit results corresponding to the analysis of $B \to D^* \ell \bar{\nu}_\ell$ alone in Table V. We fit $C_T = C_s^2 + C_p^2$ along with $|V_{cb}|$ and the BGL coefficients for different values of $\Lambda$ between 1 and 10. However, we present the results for only three different values of the cutoff scale $\Lambda$, e.g., $\Lambda = 1$, 2, and 5 TeV. In the cases we study with different values of $\Lambda$, the fitted values for the BGL coefficients are identical, and we only present the results for $\Lambda = 1$ TeV. Note that because of the new contribution in the decay rate distribution, there is a small shift ($\approx 5.5\%$) in the best-fit values of $|V_{cb}|$. However, the fitted values are consistent within $1\sigma$ with the one obtained without any NP (Table I). We obtain a nonzero solution for $C_T$, which is allowed due to a small discrepancy between the Fermilab-MILC estimates and the measurement of the decay rates, which can be seen in Fig. 8 of Ref. [38].

TABLE V. Fit result for $|V_{cb}|$ and $C_T$ (GeV$^{-2}$) from the frequentist analysis for different NP scenarios with the same $B \to D^* \ell \bar{\nu}_\ell$ data set as in Table I. We only show the fit results for the BGL coefficients for $\Lambda = 1$ TeV; the results for $\Lambda = 2$ and 5 TeV are identical.

| | Fit quality | | | |
|---|---|---|---|---|
| Scale $\Lambda$ (TeV) | $\chi^2$/d.o.f. | $p$-value | Parameter | Fit result |
| 1.0 | 42.57/44 | 53.31% | $C_T$ (GeV$^{-2}$) | 0.306(85) |
| | | | $\|V_{cb}\|$ | $40.82(93) \times 10^{-3}$ |
| | | | $a_0^f$ | 0.0122(1) |
| | | | $a_1^f$ | 0.0181(96) |
| | | | $a_2^f$ | −0.268(210) |
| | | | $a_0^g$ | 0.0333(11) |
| | | | $a_1^g$ | −0.099(64) |
| | | | $a_2^g$ | −0.058(148) |
| | | | $a_1^{\mathcal{F}_1}$ | −0.0003(17) |
| | | | $a_0^{\mathcal{F}_2}$ | 0.0513(12) |
| | | | $a_1^{\mathcal{F}_2}$ | −0.185(60) |
| | | | $a_2^{\mathcal{F}_2}$ | 0.981(921) |
| 2.0 | 42.57/44 | 53.31% | $C_T$ (GeV$^{-2}$) | 0.272(75) |
| | | | $\|V_{cb}\|$ | $40.82(93) \times 10^{-3}$ |
| 5.0 | 42.57/44 | 53.31% | $C_T$ (GeV$^{-2}$) | 0.237(66) |
| | | | $\|V_{cb}\|$ | $40.82(93) \times 10^{-3}$ |

As a next step, we include the data on $B \to D^* \ell \bar{\nu}_\ell$ alongside all of the other data used in the CKM fit. The presence of a new contribution in $P \to M \ell \nu_\ell$ and $P \to \ell \nu_\ell$ decays modifies the CKM element to $|V'_{ij}| = |V_{ij}(1 \pm C_{V_2})|$ (with $C_{V_1} = 0$). In such cases, the measured values of the elements should be considered to be $|V'_{ij}|$, while $|V_{ij}|$ will be parametrized in terms of $A$, $\lambda$, $\bar{\rho}$, and $\bar{\eta}$. In the expansion of $V_{ij}$ we consider terms up to order $\lambda^8$. The fit results of the corresponding frequentist analysis are presented in Table VI.[2] Note that in the presence of NP, the fitted values of $A$, $\lambda$, $\bar{\rho}$, and $\bar{\eta}$ remain practically unchanged. For both values of $\Lambda$ the allowed ranges of $C_T$ are consistent with zero and very tightly constrained. The negative values of $C_T$ could be accommodated by introducing phases in $C_s$ and $C_p$, for example, using the following replacements: $C_s \to e^{i\pi/2} C_s = iC_s$ and $C_p \to e^{i\pi/2} C_p = iC_p$.[3]

---

[2] In Table XVI, we list the fit results for the Wolfenstein parameters including NP in the presence of the Belle 2017 data and find no significant changes in the fit results compared to those listed in Table VI.

[3] In principle, one can consider $C_s$ and $C_p$ to be complex with the respective phases as unknowns, which can be constrained from the data on mixing and electric dipole moments, etc. We do not explore this possibility here, and leave it to future work. Furthermore, it is to be noted that our NP scenario has negligible impacts on $K$-$\bar{K}$ or $B_q - \bar{B}_q$ ($q = d$, $s$) mixing.

TABLE VI. Fit results for the Wolfenstein parameters and $C_T$ with NP. For the NP analyses, we show the results for three benchmark values of the cutoff scale, $\Lambda = (1.0, 2.0, 5.0)$ TeV. The corresponding results for the BGL coefficients are given in Table X in Appendix C.

| Case | | $\chi^2$/d.o.f. | $p$-value (%) | Fit result | | | | |
|---|---|---|---|---|---|---|---|---|
| | | | | $C_T$ (GeV$^{-2}$) | A | $\lambda$ | $\bar{\rho}$ | $\bar{\eta}$ |
| Scale | 1 TeV | 87.49/70 | 7.69 | $0.00003 \pm 0.00013$ | $0.799806 \pm 0.007691$ | $0.224982 \pm 0.000293$ | $0.176546 \pm 0.009690$ | $0.386274 \pm 0.011863$ |
| | 2 TeV | 87.49/70 | 7.69 | $0.00002 \pm 0.00009$ | $0.799806 \pm 0.007691$ | $0.224982 \pm 0.000293$ | $0.176545 \pm 0.009689$ | $0.386274 \pm 0.011863$ |
| | 5 TeV | 87.49/70 | 7.69 | $0.000015 \pm 0.000066$ | $0.799808 \pm 0.007691$ | $0.224982 \pm 0.000293$ | $0.176544 \pm 0.009690$ | $0.386273 \pm 0.011863$ |

TABLE VII. Extracted values of the Wolfenstein parameters in the Bayesian fit with and without the contributions from NP. We consider the NP scale $\Lambda$ to be 1, 2, and 5 TeV in the NP scenarios. The numbers correspond to the medians and $1\sigma$ quantiles of the respective distributions for the CKM parameters. The corresponding results for the BGL coefficients are given in Table X in Appendix C.

| | | In scenarios with NP | | |
|---|---|---|---|---|
| Parameters | Without NP | $\Lambda = 1$ TeV | $\Lambda = 2$ TeV | $\Lambda = 5$ TeV |
| A | $0.79925^{+0.00766}_{-0.00757}$ | $0.79922^{+0.00767}_{-0.00753}$ | $0.79922^{+0.00765}_{-0.00753}$ | $0.79943^{+0.00769}_{-0.00759}$ |
| $\lambda$ | $0.224979 \pm 0.000293$ | $0.224979 \pm 0.000293$ | $0.22498^{+0.000294}_{-0.000292}$ | $0.224979 \pm 0.000292$ |
| $\bar{\rho}$ | $0.17657^{+0.00971}_{-0.00969}$ | $0.1765^{+0.00959}_{-0.00962}$ | $0.17658^{+0.0097}_{-0.00963}$ | $0.17628^{+0.00977}_{-0.0096}$ |
| $\bar{\eta}$ | $0.3867^{+0.0119}_{-0.0118}$ | $0.3866^{+0.0118}_{-0.0117}$ | $0.3865^{+0.0119}_{-0.0118}$ | $0.3862^{+0.0119}_{-0.0118}$ |
| $C_T$ (GeV$^{-2}$) | NA | $0.0000297^{+0001260}_{-0001263}$ | $0.0000214 \pm 0.0000906$ | $0.0000156^{+0.0000659}_{-0.000065}$ |

In the Bayesian view of subjective probability, all unknown parameters are treated as uncertain and thus should be described in terms of their underlying probability distributions. In addition to the frequentist analysis, we also carry out a Bayesian fit for the Wolfenstein parameters with and without the contribution from the NP cases discussed above. The results of the Bayesian fit are given in Table VII. Note that the fit values of the Wolfenstein parameters are highly consistent in all of the scenarios with and without the NP. All other observations are similar to the ones obtained in the frequentist analysis. In order to provide numerical estimates, we present the median and the corresponding $1\sigma$ quantiles for the posteriors of the respective parameters. In the presence of the NP, the best-fit points of all of the Wolfenstein parameters are almost unchanged. The fitted values for $C_T$ are given in Table VII. The corresponding one-dimensional posterior is shown in Fig. 5. In accordance with our expectations, $C_T$ is consistent with zero, and we obtain tight constraints on it which become more stringent with increasing values of the cutoff scale. The overall observations remain similar to those obtained from the frequentist analysis. The posteriors for the Wolfenstein parameters $A$, $\lambda$, $\bar{\rho}$, and $\bar{\eta}$ are understandably Gaussian. We refrain from showing the corresponding posteriors for all of the fit and nuisance parameters here. For the Bayesian analysis related to the BGL parameters, we provide the corresponding information consisting of the one-dimensional posteriors, two-dimensional correlation plots, and the corresponding numerical estimates as a triangle plot (Fig. 12) in Appendix A.

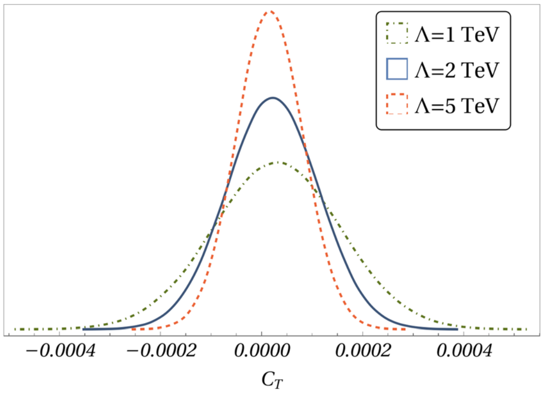

FIG. 5. One-dimensional posteriors for the NP coupling $C_T$ corresponding to the NP scale $\lambda$ taken to be 1, 2, and 5 TeV.

In Fig. 6, we provide two-dimensional correlation plots between the CKM parameters $A - \lambda$, $\bar{\rho} - \bar{\eta}$, and $A - \bar{\rho}$. We also display the correlation of the NP parameter $C_T$ with $A$, $\bar{\eta}$, and $\bar{\rho}$. Note that in the presence of a new contribution the correlations between $A$, $\lambda$, $\bar{\eta}$, and $\bar{\rho}$ do not change. Also, for all values of the scale $\Lambda$, $C_T$ has negligible correlations with the Wolfenstein parameters. In addition, we have checked that $C_T$ has a negligible correlation with $\lambda$ for all cases. The numerical values of these correlations are presented in Appendix A. In the absence of any NP contributions, the numerical values of the correlations are given in Tables XI–XIV.

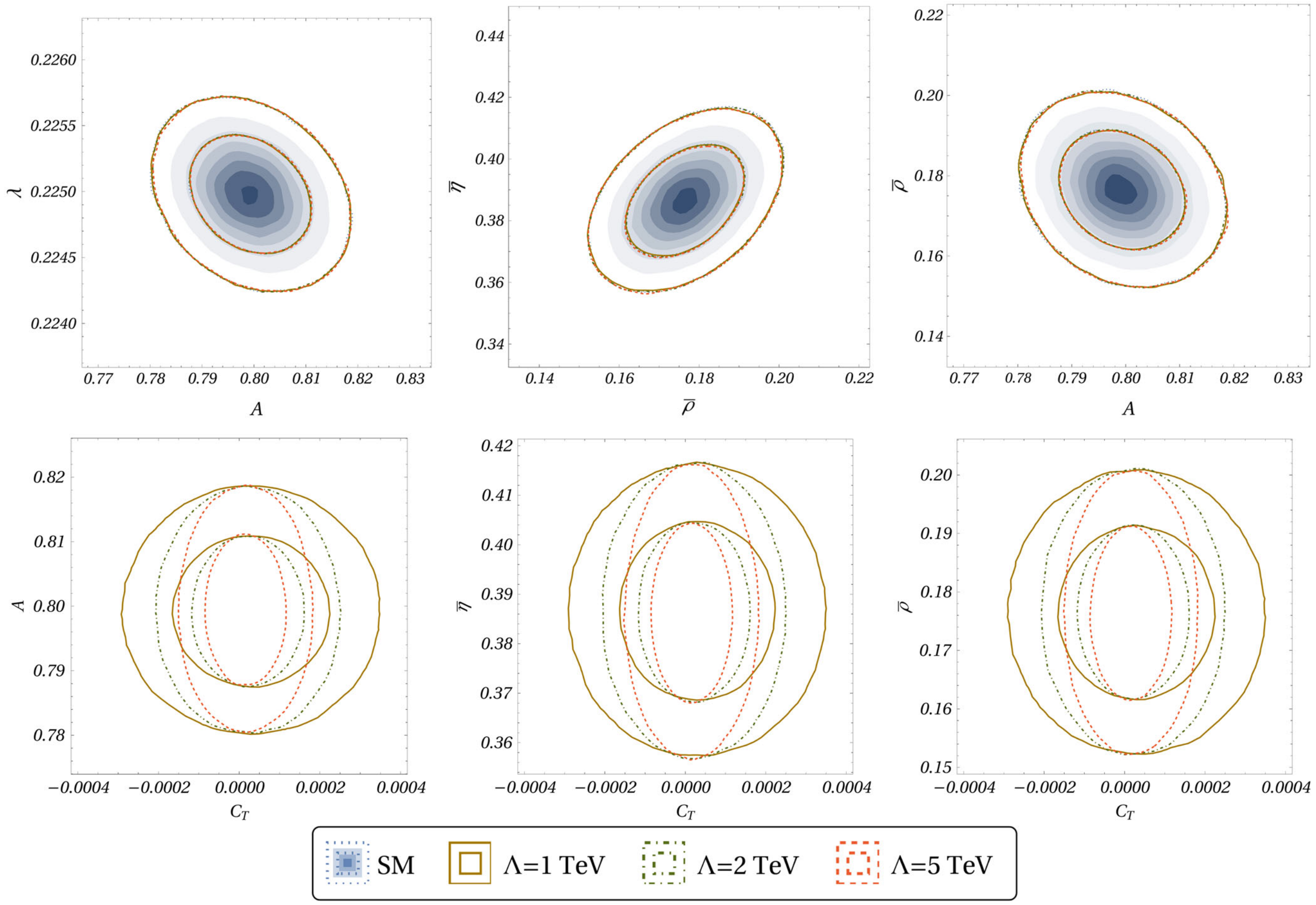

FIG. 6. Two-dimensional correlation plots for the Wolfenstein parameters. We show the correlations between $A-\lambda$, $\bar{\rho}-\bar{\eta}$, and $A-\bar{\rho}$ for the scenario without NP and the two NP cases with the NP scale $\Lambda$ taken to be 1, 2, and 5 TeV. The smaller and larger concentric ellipses represent the $1\sigma$ and $2\sigma$ regions and are displayed for the SM and all of the NP cases. The shaded contours represent probability densities and are provided only for the SM case. The blue (dotted) ellipses represent the SM, while the brown (solid), green (dot-dashed), and red (dashed) ellipses represent the NP cases with $\Lambda = 1$, 2, and 5 TeV, respectively.

TABLE VIII. Extracted values of the CKM elements from the fit results given in Table VII in the different scenarios with and without the NP. These estimates have been obtained from the Bayesian posteriors of the respective runs for the SM and NP scenarios with the NP scale $\Lambda$ taken to be 1, 2, and 5 TeV. The numbers correspond to the medians and $1\sigma$ quantiles of the respective distributions for the CKM elements. It is evident that the inclusion of NP has a negligible effect on these elements.

| | | In scenarios with NP | | |
|---|---|---|---|---|
| CKM elements | Without NP | $\Lambda = 1$ TeV | $\Lambda = 2$ TeV | $\Lambda = 5$ TeV |
| $\lvert V_{ud}\rvert$ | $0.974355 \pm 0.000068$ | $0.974356 \pm 0.000068$ | $0.974355^{+0.000067}_{-0.000068}$ | $0.974356 \pm 0.000067$ |
| $\lvert V_{us}\rvert$ | $0.22498 \pm 0.00029$ | $0.22498 \pm 0.00029$ | $0.22498 \pm 0.00029$ | $0.22498 \pm 0.00029$ |
| $\lvert V_{ub}\rvert$ | $0.00397 \pm 0.00011$ | $0.00397 \pm 0.00011$ | $0.00397 \pm 0.00011$ | $0.00396 \pm 0.00011$ |
| $\lvert V_{cd}\rvert$ | $0.22486 \pm 0.00029$ | $0.22486 \pm 0.00029$ | $0.22486 \pm 0.00029$ | $0.22486 \pm 0.00029$ |
| $\lvert V_{vs}\rvert$ | $0.97351 \pm 0.00007$ | $0.973509 \pm 0.00007$ | $0.973509 \pm 0.00007$ | $0.973509^{+0.000069}_{-0.00007}$ |
| $\lvert V_{cb}\rvert$ | $0.04045^{+0.00038}_{-0.00037}$ | $0.04045 \pm 0.00037$ | $0.04045 \pm 0.00037$ | $0.04046^{+0.00038}_{-0.00037}$ |
| $\lvert V_{td}\rvert$ | $0.00828 \pm 0.0001$ | $0.00828 \pm 0.0001$ | $0.00828 \pm 0.0001$ | $0.00828 \pm 0.0001$ |
| $\lvert V_{ts}\rvert$ | $0.0398^{+0.00037}_{-0.00036}$ | $0.03979 \pm 0.00036$ | $0.03979 \pm 0.00036$ | $0.0398^{+0.00037}_{-0.00036}$ |
| $\lvert V_{tb}\rvert$ | $0.999174 \pm 0.000015$ | $0.999174 \pm 0.000015$ | $0.999174 \pm 0.000015$ | $0.999173 \pm 0.000015$ |

TABLE IX. $R(D^*)$ estimates for the SM and the three NP scenarios with scales of 1, 2, and 5 TeV. The Bayesian estimates correspond to the median and $1\sigma$ quantiles for the respective distributions for $R(D^*)$.

| | | | In scenarios with NP | | |
|---|---|---|---|---|---|
| Observable | | SM | 1 TeV | 2 TeV | 5 TeV |
| $R(D^*)$ | Frequentist | $0.2579 \pm 0.0034$ | $0.2579 \pm 0.0034$ | $0.2579 \pm 0.0034$ | $0.2579 \pm 0.0034$ |
| | Bayesian | $0.2586^{+0.0031}_{-0.0030}$ | $0.2586^{+0.0031}_{-0.0030}$ | $0.2586^{+0.0031}_{-0.0030}$ | $0.2586^{+0.0031}_{-0.0030}$ |

As mentioned earlier, in the presence of new contributions the CKM element $V_{ij}$ is modified to $V'_{ij} = V_{ij}(1+\Delta_{\rm NP})$. To check the impact of the NP on the extracted values of the CKM elements, we extract $V_{ij}$ in the fit with $\Delta_{\rm NP} = 0$ and compare it with the extracted values obtained from the fit results with $\Delta_{\rm NP} \neq 0$. The numerical estimates for all nine CKM parameters in all of the fit scenarios are given in Table VIII. Each of the numbers corresponds to the median and $1\sigma$ quantiles for the respective distributions of the CKM parameters. As expected, the extracted values remain unaltered in the presence of the NP effects we are considering.

As discussed in Sec. IV A, we analyze the $B \to D^*\ell\nu_\ell$ ($\ell = e$ and $\mu$) decay mode independently and along with all of the other inputs used to extract the Wolfenstein parameters. With the updated inputs from lattice calculations, we carry out fits in the SM (without any new contribution) and include new contributions. In the frequentist and Bayesian analyses, the fit results for the BGL coefficients with and without $C_T$ are given in Table X. For the semileptonic $P \to M$ decay modes we can define observables like $R(M^{(*)}) = \frac{\mathcal{B}(P\to M^{(*)}\tau\nu_\tau)}{\mathcal{B}(P\to M^{(*)}\ell\nu_\ell)}$. In the SM, these observables are expected to respect lepton universality, which can be violated in the presence of new interactions affecting these decays. For the type of new effects we are considering here, the NP effects will cancel along with the CKM elements in $R(M)$. However, in $R(M^*)$, the new contributions will affect the decay rate distributions along with the vertex factor and the contribution will be sensitive to the lepton mass. Therefore, for $R(D^*)$, the new effects will not get cancelled completely. We also take this opportunity to update the SM prediction for $R(D^*)$ with the newly available inputs. Using the results given in Table X along with the respective correlations, we predict $R(D^*)$ in the SM and in NP scenarios with three masses, which are shown in Table IX. The SM predictions are unchanged due to NP in $B \to D^*\ell\nu_\ell$, which are tightly constrained from the CKM fit analysis.

As we mentioned earlier, the extraction of $C_T$ from the detailed analysis of the inclusive $B \to X_c\ell\nu_\ell$ decays is beyond the scope of this paper. In spite of the difficulties in the extraction of NP parameters from inclusive measurements, we attempt to naively extract the allowed range of $C_T$ from the respective decay rate. Following the simplified approach discussed in Ref. [63], we define the approximate inclusive branching fraction in the presence of leading-order (LO) NP effect only in the rates

$$\mathcal{B}(B \to X_c e\nu)_{\rm exp} \approx \mathcal{B}(B \to X_c e\nu)_{\rm SM} \frac{\Gamma(B \to X_c e\nu)^{\rm LO}_{\rm NP}}{\Gamma(B \to X_c e\nu)^{\rm LO}_{\rm SM}}, \tag{27}$$

where $\mathcal{B}(B \to X_c e\nu)_{\rm exp} = (10.8 \pm 0.4)\%$ [28] is the experimentally measured branching fraction. The expressions for $\Gamma(B \to X_c e\nu)^{\rm LO}_{\rm NP}$ and $\Gamma(B \to X_c e\nu)^{\rm LO}_{\rm SM}$ can be found in Ref. [63]. Note that $\Gamma(B \to X_c e\nu)^{\rm LO}_{\rm NP}$ is sensitive to $C_T$. We can express $\mathcal{B}(B \to X_c e\nu)_{\rm SM}$ as

TABLE X. SM and NP estimates for the BGL parameters. The NP estimates are shown for both cases with the NP scale $\Lambda = 1$, 2, and 5 TeV. The Bayesian estimates correspond to the median and $1\sigma$ quantiles of the posteiors for the respective parameters.

| | Frequentist | | | | Bayesian | | | |
|---|---|---|---|---|---|---|---|---|
| Parameters | SM | $\Lambda = 1$ TeV | $\Lambda = 2$ TeV | $\Lambda = 5$ TeV | SM | $\Lambda = 1$ TeV | $\Lambda = 2$ TeV | $\Lambda = 5$ TeV |
| $a_0^f$ | $0.01219 \pm 0.00012$ | $0.01219 \pm 0.00012$ | $0.01219 \pm 0.00012$ | $0.01219 \pm 0.00012$ | $0.01218 \pm 0.00012$ | $0.01218 \pm 0.00012$ | $0.01218 \pm 0.00012$ | $0.01219 \pm 0.00012$ |
| $a_1^f$ | $0.0203 \pm 0.0092$ | $0.0202 \pm 0.0092$ | $0.0202 \pm 0.0092$ | $0.0202 \pm 0.0092$ | $0.0222 \pm 0.008$ | $0.0221^{+0.008}_{-0.0081}$ | $0.022^{+0.0081}_{-0.008}$ | $0.0214^{+0.0077}_{-0.0079}$ |
| $a_2^f$ | $-0.49 \pm 0.19$ | $-0.49 \pm 0.19$ | $-0.49 \pm 0.19$ | $-0.49 \pm 0.19$ | $-0.53 \pm 0.17$ | $-0.53 \pm 0.17$ | $-0.52 \pm 0.17$ | $-0.51 \pm 0.16$ |
| $a_0^g$ | $0.0313 \pm 0.00095$ | $0.0313 \pm 0.00095$ | $0.0313 \pm 0.00095$ | $0.0313 \pm 0.00095$ | $0.03121 \pm 0.00094$ | $0.03122 \pm 0.00094$ | $0.03121 \pm 0.00094$ | $0.03124^{+0.00095}_{-0.00094}$ |
| $a_1^g$ | $-0.142 \pm 0.062$ | $-0.143 \pm 0.062$ | $-0.143 \pm 0.062$ | $-0.143 \pm 0.062$ | $-0.149 \pm 0.036$ | $-0.147^{+0.035}_{-0.037}$ | $-0.146^{+0.035}_{-0.037}$ | $-0.154^{+0.037}_{-0.036}$ |
| $a_2^g$ | $-0.43 \pm 1.44$ | $-0.41 \pm 1.44$ | $-0.41 \pm 1.44$ | $-0.41 \pm 1.44$ | $-0.13^{+0.68}_{-0.58}$ | $-0.22^{+0.7}_{-0.54}$ | $-0.25^{+0.77}_{-0.49}$ | $0.022^{+0.627}_{-0.685}$ |
| $a_1^{\mathcal{F}_1}$ | $0.0017 \pm 0.0014$ | $0.0017 \pm 0.0014$ | $0.0017 \pm 0.0014$ | $0.0017 \pm 0.0014$ | $0.0022 \pm 0.0012$ | $0.0022 \pm 0.0012$ | $0.0022 \pm 0.0012$ | $0.0021 \pm 0.0012$ |
| $a_0^{\mathcal{F}_2}$ | $0.0508 \pm 0.0012$ | $0.0508 \pm 0.0012$ | $0.0508 \pm 0.0012$ | $0.0508 \pm 0.0012$ | $0.0507^{+0.0012}_{-0.0011}$ | $0.0507^{+0.0012}_{-0.0011}$ | $0.0507 \pm 0.0012$ | $0.0508^{+0.0012}_{-0.0011}$ |
| $a_1^{\mathcal{F}_2}$ | $-0.149 \pm 0.058$ | $-0.149 \pm 0.058$ | $-0.149 \pm 0.058$ | $-0.149 \pm 0.058$ | $-0.125^{+0.033}_{-0.028}$ | $-0.127^{+0.032}_{-0.028}$ | $-0.126^{+0.033}_{-0.028}$ | $-0.134^{+0.028}_{-0.026}$ |
| $a_2^{\mathcal{F}_2}$ | $0.99 \pm 0.9$ | $0.99 \pm 0.9$ | $0.99 \pm 0.9$ | $0.99 \pm 0.9$ | $0.61^{+0.28}_{-0.49}$ | $0.63^{+0.27}_{-0.44}$ | $0.62^{+0.28}_{-0.45}$ | $0.76^{+0.18}_{-0.38}$ |

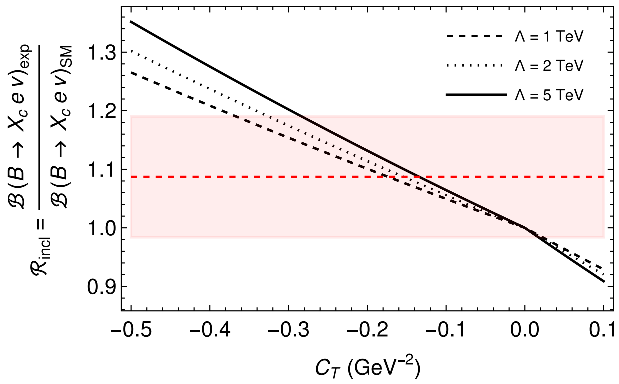

FIG. 7. Variation of $\mathcal{R}_{\rm incl}$ as a function of the NP coupling $C_T$ for three different values of the scale Λ. The red dashed line represents the central value of the ratio with the $1\sigma$ uncertainty depicted by the shaded region.

$$\mathcal{B}(B\to X_c e\nu)_{\rm SM} = \tau_B |V_{cb}|^2_{\rm incl}\Gamma'. \qquad (28)$$

Here, $\tau_B$ is the mean lifetime of the $B$ meson, and $\Gamma'$ is the integrated rate and includes all of the available higher-order perturbative corrections up to $\mathcal{O}(\alpha_s^3)$ and the corrections to the nonperturbative matrix elements; for details, see Refs. [30,54]. Note that $\Gamma'$ is a function of $m_b^2$, $m_c^2$, and different nonperturbative matrix elements which could be extracted from a fit to the respective leptonic energy moments and the moments of the hadronic invariant mass of the respective differential distributions [29,30]. Using these fitted parameters, one can determine $\Gamma'$ and thereby extract $|V_{cb}|$ from Eq. (28) by letting $\mathcal{B}(B\to X_c e\nu)_{\rm SM} = \mathcal{B}(B\to X_c e\nu)_{\rm exp}$. Following this approach, the authors of Ref. [54] obtained $\Gamma' = 2.44(11)\times 10^{-11}$ GeV, and hence $|V_{cb}|_{\rm incl} = 42.16(51)\times 10^{-3}$. Note that the fit in Ref. [54] did not assume contributions from NP.

In this analysis, we aim to constrain the magnitude of $C_T$ from Eq. (27) with the measured value $\mathcal{B}(B\to X_c e\nu)_{\rm exp}$, and the $|V_{cb}|$ obtained from the CKM fit without any inputs from the inclusive decays. Ideally, one should simultaneously fit the $|V_{cb}|$ along with $C_T$; however, for the naive estimate, the only available input is the inclusive branching fraction. Therefore, we must fix $|V_{cb}|$ from the other measurements. In order to extract the allowed range of $C_T$, we calculate the ratio

$$\mathcal{R}_{\rm incl} = \frac{\mathcal{B}(B\to X_c e\nu)_{\rm exp}}{\mathcal{B}(B\to X_c e\nu)_{\rm SM}} = 1.087 \pm 0.034. \qquad (29)$$

With the fitted $\Gamma' = 2.44(11)\times 10^{-11}$ GeV, along with our predicted $|V_{cb}| = 0.04045^{+0.00038}_{-0.00037}$ from the CKM fit (Table VIII), we find $\mathcal{B}(B\to X_c e\nu)_{\rm SM} = (9.9\pm 0.5)\%$ which is consistent with the measured value $\mathcal{B}(B\to X_c e\nu)_{\rm exp}$ at 68% C.L. Note that from Eq. (27) we can define $\mathcal{R}_{\rm incl} \approx \frac{\mathcal{B}(B\to X_c e\nu)^{\rm LO}_{\rm NP}}{\mathcal{B}(B\to X_c e\nu)^{\rm LO}_{\rm SM}}$, and using the estimate in Eq. (29) we can find the allowed ranges of $C_T$. In Fig. 7, we show the variation of $\mathcal{R}_{\rm incl}$ with $C_T$, from which we can get the allowed range of $C_T$ required to explain $\mathcal{R}_{\rm incl}$ in its estimated range. The figure shows the estimated $1\sigma$ limit of the ratio $\mathcal{R}_{\rm incl}$, and the allowed magnitude of $C_T$ could be as large as 0.2. As expected, the inclusive measurement does not provide a strong constraint on $C_T$, and even though large negative values of $C_T$ are favored, the corresponding range obtained is consistent with 0.

### D. DM phenomenology

We point out the main results from DM phenomenology in this section. Before we present our results related to DM phenomenology, we would like to point out different contributions to the relic density in the different mass regions of the DM ($M_\chi$), the mediator ($M_s$), and quarks. This exercise will be important given the mass hierarchy between $M_\chi$, $M_s$, and the top-quark mass. In the simplified dark matter model we are considering, for $M_\chi < M_s < m_t$, the dominant annihilation channels that will contribute to relic are given by $\chi\bar{\chi}\to b\bar{b}, c\bar{c}, gg$. Here, $\chi\bar{\chi}\to gg$ is a one-loop process where the dominant contribution to the effective $S\to gg$ vertex will be from a top-quark loop [14,64]. However, for $M_\chi > m_t$, the dominant annihilation channel is $\chi\bar{\chi}\to t\bar{t}$ due to the quark mass dependence of the mediator-quark couplings. At and above the top threshold, i.e., when $M_s \gtrsim 2m_t$, resonant annihilation into top-quark pairs is sufficient to generate the observed relic abundance. Finally, when $M_\chi > M_s$, the annihilation will dominantly proceed via $t$-channel exchange, $\chi\bar{\chi}\to SS$. Also, in a situation when $M_\chi > m_t, M_s$ and $M_s > 2m_t$, there will be contributions to relic from both the $s$-channel $\chi\bar{\chi}\to t\bar{t}$ and $t$-channel $\chi\bar{\chi}\to SS$ annihilation.

Considering the facts discussed above, in the context of DM phenomenology, we present the analysis in two segments for better understanding: one for $M_s < 2m_t$ and the other for $M_s \gtrsim 2m_t$. We first begin by showing the allowed parameter space satisfying the relic data in the presence of scalar couplings only, i.e., when $g_p = g_p' = 0$ and $g_s, g_s' \neq 0$, in the left panel of Fig. 8. The allowed values of $g_s$ can be inferred from the fit result for $C_T$ (with $C_p = 0$), as listed in Table VI. For simplicity, we only consider the allowed solutions for $C_T$ that are positive in the $2\sigma$ range of the best-fit estimate for the DM analysis. Therefore, we have $g_s = \sqrt{v^2 C_T}$, while $g_s'$ varies between 0–10. Note that the allowed value of $g_s$ is restricted to $\lesssim 4$. In the left panel of Fig. 8 we show the correlation between the two scalar couplings satisfying the relic abundance of dark matter with a mass of 200 GeV and mediator masses of 300, 500, 1000 GeV (dark magenta, dark blue, and dark orange lines, respectively). However, we find that the scalar

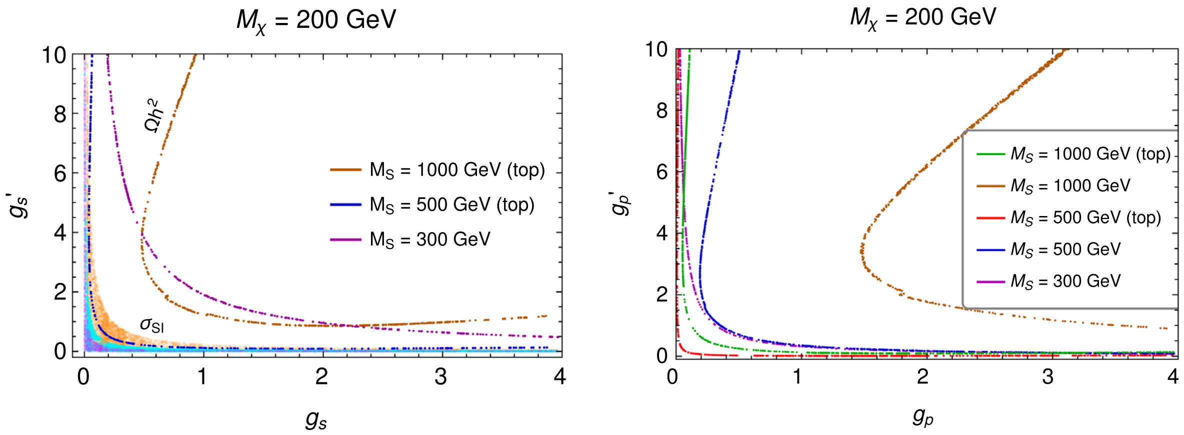

FIG. 8. Left: parameter space in the $g_s$-$g_s'$ plane satisfying the DM relic constraints for a mediator of mass 0.3 TeV (dark magenta), 0.5 TeV (dark blue), and 1 TeV (dark orange) for $M_\chi = 200$ GeV in the absence of pseudoscalar couplings. The dark matter is underabundant in the region to the right of these curves. We also show the region allowed by the Xenon-1T data on the spin-independent dark matter–nucleon scattering cross section as lighter shades of the same colors. Right: a similar plot in the $g_P$-$g_P'$ plane in the absence of scalar couplings.

couplings required to satisfy the relic abundance are ruled out from the spin-independent direct-detection (SIDD) constraints from the XENON-1T experiment [65]. The regions allowed by the XENON data for the same DM and mediator masses as above are shown in light magenta, light blue, and light orange, respectively, which are far away from the allowed relic curves. Hence, for all nonzero values of the scalar couplings $g_s$ and $g_s'$, the SIDD bound plays the most important role in constraining their upper limits. The same conclusion holds for values of DM masses other than $M_\chi = 200$ GeV. Therefore, one can reestablish the fact that scalar portal DM candidates are not favored by the data.

Similarly, we show the correlations between the pseudoscalar couplings $g_p$ and $g_p'$ in the right panel of Fig. 8 for similar DM and mediator masses. Here, we set $g_s = g_s' = 0$ and obtain the bound on $g_p$ from the results of Table VI using the relation $g_p = \sqrt{v^2 C_T}$, while $g_p'$ varies between 0–10. In Fig. 9 we show the variation of the maximum of the $1\sigma$ and $2\sigma$ allowed values of the coupling $g_p$ (with $g_s \approx 0$) with the cutoff scale $\Lambda$. There are slight reductions in the allowed upper limit of the coupling with increasing values of the cutoff scale for $\Lambda \lesssim 5$ TeV. The changes in the allowed values of the coupling are almost negligible for $\Lambda > 5$ TeV. This is due to the logarithmic dependence of the coupling on the cutoff scale. Note that for mediator masses below the top threshold (for example with $M_S = 300$ GeV) the allowed values of $g_p'$ is $\lesssim 1$ and its value could be $> 1$ only if $g_p \ll 1$. Also, for $g_p \gtrsim 0.5$ the allowed values of $g_p'$ will be $\ll 1$. The constraints are severe for values of $M_S$ larger than $2m_t$ (top threshold). Such an observation is also true for the scalar coupling case discussed previously. We show the correlation between the couplings for $M_S = 1000$ and 1500 GeV. It should be noted that, if kinematically allowed, i.e., for $M_S > 2m_t$, the DM can annihilate into a pair of top quarks whose cross sections are enhanced due to the heavy top mass effect in the interaction [see Eq. (5)]. If we neglect the top-quark interaction, the resulting correlation is presented by the blue and brown curves in the right panel of Fig. 8 for $M_S = 0.5$ and 1 TeV, respectively. Larger couplings are allowed if annihilation to only light quarks is considered. In the absence of the scalar couplings, the parameter space is free of any constraints from the DM-nucleon scattering data since the pseudoscalar couplings give rise to velocity-suppressed spin-dependent scattering.

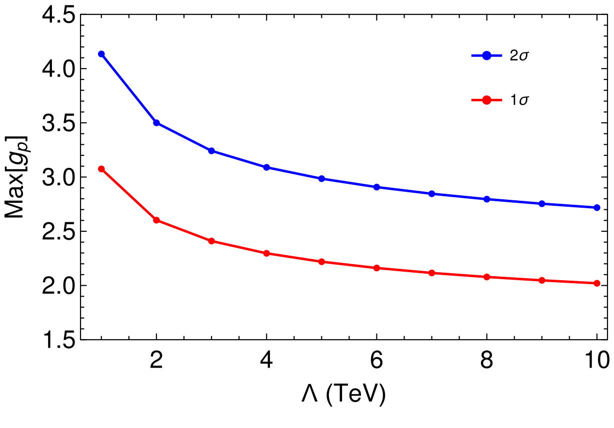

FIG. 9. Variation of the maximum $1\sigma$ and $2\sigma$ allowed values of the coupling $g_p$ when $g_s \approx 0$ or is negligibly small, with the cutoff scale.

So far, we have focused on a particular DM mass. We will discuss the phenomenology for varying mediator and DM masses in what follows. The variation of the relic abundance with the DM mass is shown in Fig. 10. Here we show the variation with the DM mass for $M_S = 0.3$, 0.5, 1.0, and 1.5 TeV using green, orange, blue, and magenta points, respectively, for the scenario

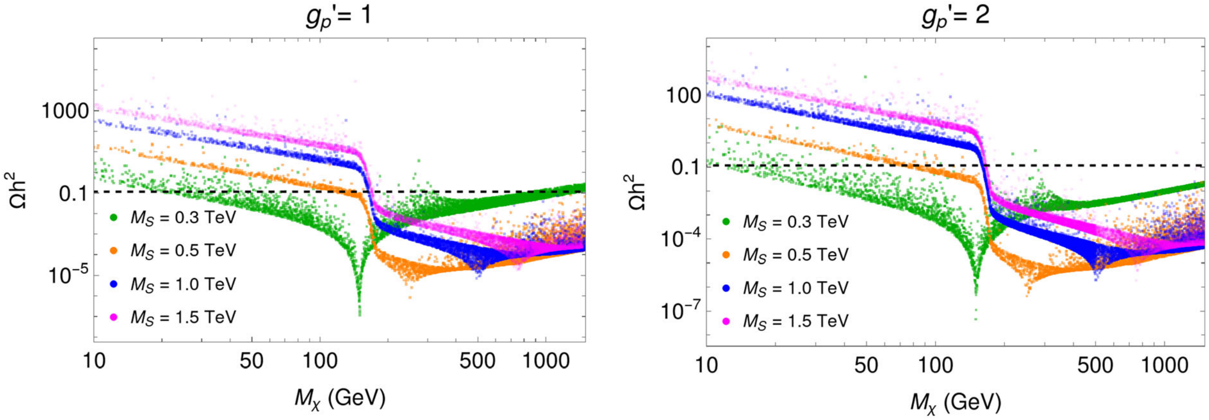

FIG. 10. Relic abundance as a function of the DM mass for the four values of $M_S$, as denoted by the green, orange, blue, and magenta points, for $0 \le g_p \le 4$ and when $g_{p'}$ is taken to be 1 (left) or 2 (right). See text for more details.

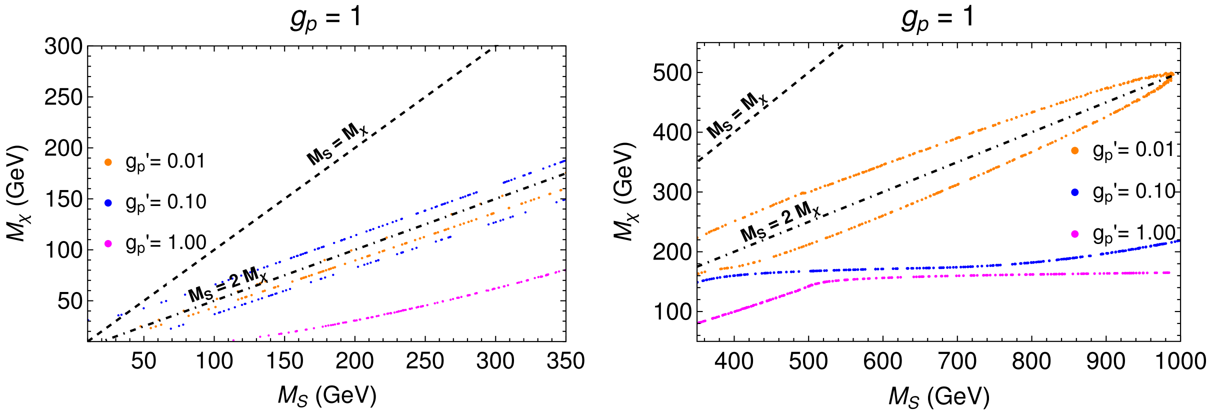

FIG. 11. Relic allowed regions in the $M_\chi$-$M_S$ plane for different values of pseudoscalar couplings when $M_S < 2m_t$ (left) and $M_S > 2m_t$ (right).

$0 \le g_p \le 4$ (as obtained above) and for $g_p' = 1$ (left panel) or 2 (right panel). The black dashed line signifies the present-day relic abundance of DM. For $g_p' = 1$, from the scans, we find that for relatively lighter masses, like $M_S = 300$ GeV, the correct relic abundance is satisfied for a wide range of DM masses on both sides of $M_S \approx 2M_\chi$. However, for values of $M_S$ higher than the top threshold, the allowed DM masses become constrained to a small region, and they satisfy $M_\chi \ll M_S/2$. A similar plot for $g_p' = 2$ is shown in the right panel of Fig. 10. One can note that the probability of getting an allowed solution for $M_\chi > M_S/2$ has decreased compared to that for $g_p' = 1$. Therefore, for higher values of the coupling $g_p'(> 2)$, the relic abundance will be satisfied only when $M_\chi < M_S/2$. On the other hand, one would expect the solution to be concentrated near $M_\chi \approx M_S/2$ for values of $M_S$ near or below the top threshold and $g_p' < 1$.

In Fig. 11, we show the allowed correlations between the mediator and dark matter masses for a few values of $g_{p'}$, while we fix $g_p = 1$. The relic abundance is satisfied only along the orange, blue, and magenta curves for $g_{p'} = 0.01$, 0.1, and 1.0, respectively. These benchmark values were chosen after an inspection of the correlations in Fig. 8. The plot to the left corresponds to mediator masses $M_S \lesssim 2m_t$ GeV while the one to the right represents the cases where $M_S \gtrsim 2m_t$ . The black dashed and dot-dashed lines depict $M_\chi = M_S$ and $M_\chi = 2M_S$, respectively. It is evident from the plots that for $M_S < 2m_t$, for lower values of $g_p'(\lesssim 1)$, the relic abundance is satisfied near the region $M_\chi \approx M_S/2$. However, for a relatively high value like $g_p' \approx 1$, the relic abundance will be satisfied only when $M_\chi < M_S/2$. For $M_S > 2m_t$, for smaller values of $g_p'$ (for example, $g_p' = 0.01$), the relic abundance will be satisfied near the region $M_\chi \approx M_S/2$. However, as observed earlier, the relic abundance will be satisfied for $M_\chi < M_S/2$ when $g_p'$ is not too small. High DM masses ($\gtrsim$350 GeV) do not satisfy the relic constraint until the annihilation to the top final state becomes relevant. This is expected since the annihilation cross section is smaller for low values of the couplings, thereby making the relic overabundant. Therefore, we need smaller DM masses to tune the relic abundance to the correct amount by increasing the overall cross section. The reverse is true for the cases shown in the right panel of Fig. 11 since the top-quark effect is so dominant that high DM masses are disfavored unless the couplings are very low.

Based on the analyses of 8 TeV data, the relevant bounds on $g_s, g'_s, g_p, g'_p, M_S$, and $M_\chi$ from the collider searches $\not{E}_T+$ jet and $\not{E}_T + \bar{t}t$ can be found in Refs. [14] and [64], respectively. The corresponding bounds have been updated in the newly available analyses from the ATLAS [66] and CMS [67–70] collaborations, which are based on the data at the center-of-mass energy $\sqrt{s} = 13$ TeV. Although a dedicated collider analysis is beyond our paper's scope or motivation, we can draw some inferences from the results of the ATLAS and CMS collaborations on the respective model parameters. The ATLAS and CMS collaborations looked for signatures in $X + \not{E}_T$ final states, where $X$ stands for $W/Z/\gamma$ or jets. Note that the LHC bounds are only applicable for $M_s \gtrsim 2M_\chi$. As was seen in these experimental analyses, the strong constraints on the scalar or pseudoscalar mediator masses come mainly from the analyses of $(t/\bar{t}/t\bar{t} + \not{E}_T)$ [67,69] and $\not{E}_T +$ jets signatures [66,70]. As can be seen from Ref. [69], from the analysis of combined events in $(t/\bar{t}/t\bar{t} + \not{E}_T)$ searches for $g_p = g'_p = 1$ and the DM mass $M_\chi = 1$ GeV, mediator masses $M_s < 300$ GeV are excluded at 95% C.L. On the other hand, at both CMS and ATLAS [66,70], from the searches of the energetic jets and large missing transverse energy, constraints are obtained on $M_s$ for $M_\chi = 1$ GeV with the magnitude of the mediator couplings: $g_p \approx 1.5$ and $g'_p = 1$.[4] Their studies exclude pseudoscalar mediator mass $M_s$ up to 470 GeV at 95% C.L. As proposed in Ref. [71], the constraints are obtained in the $M_s$-$M_\chi$ plane from the LHC analyses for fixed values of the mediator couplings, which can be seen from Ref. [66], and it could be helpful to exclude a part of the region of low DM masses.

In addition, we understand that the jets plus missing transverse energy production cross section will increase with increasing values of $g_p$ or $g'_p$. One should note that the maximum excluded values of $M_s$ decrease with increasing $M_\chi$, as the value of the branching fraction of the mediator to DM particle decays diminishes [71]. Therefore, with increasing values of the DM masses, the bounds on the mediator masses will be less stringent. Also, the naive expectation is that the mediator production cross sections will decrease with increasing values of $M_s$. Therefore, it is expected that for higher values of $M_\chi$ and $M_s$ ($\gtrsim$470 GeV), the mediator coupling $g_p > 1.5$ will be allowed by the LHC data. Also, the current LHC bound on $M_s$ will be relaxed for $g_p$ or $g'_p < 1$. In our analysis, we obtain the relic allowed regions for $g_p = g'_p = 1$ shown in magenta in Fig. 11 for $M_s \lesssim 350$ GeV (left panel), which will not be allowed by the LHC data. In the same figure, the other allowed solutions are shown for $g'_p = 0.1$ and 0.01, which might still be allowed by the current experimental searches. For $g'_p = 0.1$ or 0.01, due to the reduction in the production cross section, the exclusion limit on $M_s$ will be less stringent than that obtained for $g'_p = 1$. Also, the allowed regions shown in the right panel of Fig. 11 for $M_s > 400$ GeV will be allowed by the current LHC limits. A dedicated collider analysis may be required to support these arguments, which is beyond the scope of this paper. Also, the current collider searches have not ruled out the upper limits on the values of $g_s$ or $g_p$ obtained from the CKM fit. The variation of the maximum allowed value for $g_p$ with the cutoff scale have been shown in Fig. 9, a more stringent bound from the future collider experiment may be helpful to get some understanding about the viable cutoff scale. More precise data might be helpful to constrain it further both at the collider and in the CKM fit.

## V. SUMMARY

From the global CKM fit analysis, in this paper we analyzed the constraints on the parameters of a class of NP models with a neutral quark current interaction mediated by a heavy scalar. This kind of NP has an impact on the leptonic and semileptonic decays at the one-loop level. Also, with the newly available updates, we have extracted Wolfenstein parameters and the related CKM elements with and without a contribution from NP from the global fit. In this paper, we mainly focused on the impact of our bounds on DM phenomenology. However, the bounds might be applicable in any other relevant phenomenology.

We have considered a simplified DM model with fermionic dark matter whose interactions with the SM are mediated by a heavy neutral scalar. There is no symmetry to forbid the interactions of the SM quarks with this new scalar. Hence, it will contribute to the charged-current vertices of $\bar{d}_i u_j W$ at the one-loop level. The modifications to the $P \to M$ and $P \to M^*$ transitions due to the new interactions are in contrast to each other. In case of the leptonic $P \to \ell\nu_\ell$ and semileptonic $P \to M$ decays, the vertex factors will be altered, while in case of the $P \to M^*$ semileptonic decays the $q^2$ decay distribution itself is modified. As a recent development, lattice results on the form factors of the $B \to D^*\ell\nu_\ell$ decay at nonzero recoil are now available. Therefore, we updated the SM prediction of the CKM element $|V_{cb}|$ before incorporating the NP effects. We obtained $|V_{cb}| = 38.69(79) \times 10^{-3}$ at 68% C.L. We also predicted the observable $R(D^*)$ in the different fit scenarios with and without the NP.

---

[4] Note that in Refs. [66,70] the couplings of the mediator with the quarks were defined a little differently than in our paper. The couplings are related by the relation $g_p = \frac{v}{m_t} g_{\mathrm{LHC}}$, where $m_t$ is the mass of the top quark. However, in Ref. [69] the definitions of $g_p$ and $g_s$ exactly match ours.

With this new update and all other available CKM measurements, we performed a global fit in the presence of the NP effects for some fixed values of the mediator mass. From this fit, we could only constrain the combination $C_T$ and not the individual couplings $C_s$ and $C_p$. We showed that for high values of $M_S$, the coupling gets severely constrained by the data. From the dark matter SIDD constraints, we can restrict the scalar couplings $C_s$ and $g'_s$ to minimal values. This automatically translates to a bound on the parameter $C_p$ from our fit results on $C_T$. However, since the pseudoscalar couplings have a velocity-suppressed contribution to the spin-dependent DD cross section, there remains some freedom in $g'_p$. With this setup, we discussed the relevant DM phenomenology.

## ACKNOWLEDGMENTS

This work of S. N. is supported by the Science and Engineering Research Board, Govt. of India, under the Grant CRG/2018/001260.

## APPENDIX A: FIT RESULTS FOR THE BGL COEFFICIENTS

In this appendix, we show the fitted values of the BGL coefficients (Table X) defined in Eq. (18) which are obtained from a combined fit to $B \to D^* \ell \nu_\ell$ decay rates and other relevant inputs used in global CKM fit analysis. In Fig. 12, we provide the triangle plot for the BGL parameters corresponding to the SM in this section which are almost unchanged in the presence of NP.

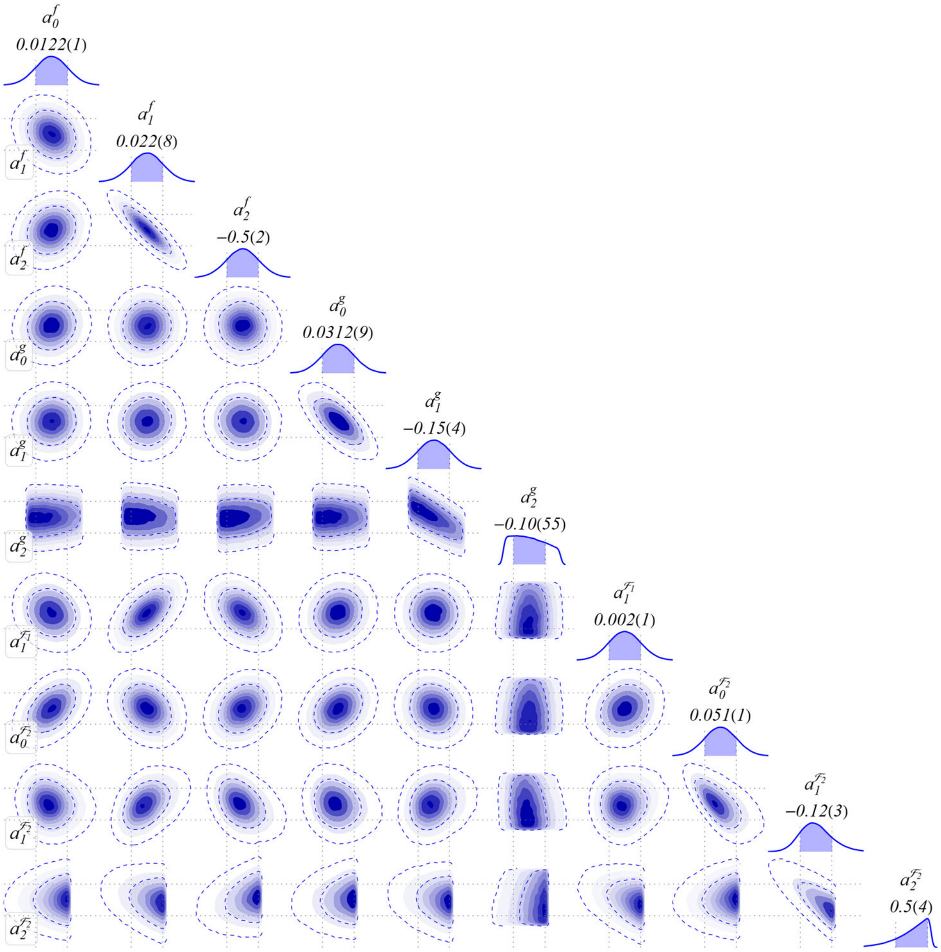

FIG. 12. Triangle plot for the BGL parameters for the SM. We find no appreciable changes for the three NP scenarios compared to the SM as far as the posterior and correlations for the BGL parameters are concerned. The central value and corresponding errors for the parameters are provided at the top of the corresponding one-dimensional posteriors.

TABLE XI. Correlations between the four Wolfenstein parameters corresponding to the fit without NP.

| SM | A | $\lambda$ | $\bar{\rho}$ | $\bar{\eta}$ |
|---|---|---|---|---|
| A | 1. | −0.258465 | −0.210554 | −0.493578 |
| $\lambda$ | −0.258465 | 1. | 0.0728912 | −0.055793 |
| $\bar{\rho}$ | −0.210554 | 0.0728912 | 1. | 0.409138 |
| $\bar{\eta}$ | −0.493578 | −0.055793 | 0.409138 | 1. |

## APPENDIX B: CORRELATIONS BETWEEN THE WOLFENSTEIN PARAMETERS AND $C_T$

In this appendix, we provide numerical estimates for the correlations between $A$, $\lambda$, $\bar{\eta}$, $\bar{\rho}$, and $C_T$ corresponding to the analyses with and without any NP contributions. In the case of NP, we present the results for the corresponding scales $\Lambda = 1$ and 2 TeV. These have been obtained from the Bayesian posteriors.

## APPENDIX C: FIT RESULTS INCLUDING BELLE 2017 DATA

In this appendix, we point out the effect on the fit results if we include the $B \to D^* \ell \nu$ data from the Belle 2017 analysis [43]. In Table XV, we list the results for the SM fit to the data for extracting $|V_{cb}|$ and the BGL form factor parameters. We can see from the table that the fit values are consistent with those obtained without considering the Belle 2017 data set given in Table I. Similarly, for the full CKM fit including NP, the fit values (as shown in Table XVI) for $C_T$ remain unchanged, while the Wolfenstein parameters remain consistent within the $1\sigma$ errors of the previous fit result.

TABLE XII. Correlations between the four Wolfenstein parameters along with $C_T$ for the NP scale $\Lambda = 1$ TeV.

| $\Lambda = 1$ TeV | $C_T$ | A | $\lambda$ | $\bar{\rho}$ | $\bar{\eta}$ |
|---|---|---|---|---|---|
| $C_T$ | 1. | −0.00380722 | 0.00172136 | 0.0017101 | 0.00245208 |
| A | −0.00380722 | 1. | −0.260845 | −0.216509 | −0.492561 |
| $\lambda$ | 0.00172136 | −0.260845 | 1. | 0.075102 | −0.0563302 |
| $\bar{\rho}$ | 0.0017101 | −0.216509 | 0.075102 | 1. | 0.405289 |
| $\bar{\eta}$ | 0.00245208 | −0.492561 | −0.0563302 | 0.405289 | 1. |

TABLE XIII. Correlations between the four Wolfenstein parameters along with $C_T$ for the NP scale $\Lambda = 2$ TeV.

| $\Lambda = 2$ TeV | $C_T$ | A | $\lambda$ | $\bar{\rho}$ | $\bar{\eta}$ |
|---|---|---|---|---|---|
| $C_T$ | 1. | −0.00117545 | 0.000992878 | 0.000133051 | 0.000899192 |
| A | −0.00117545 | 1. | −0.260192 | −0.214117 | −0.492652 |
| $\lambda$ | 0.000992878 | −0.260192 | 1. | 0.0719362 | −0.0561466 |
| $\bar{\rho}$ | 0.000133051 | −0.214117 | 0.0719362 | 1. | 0.414471 |

TABLE XIV. Correlations between the four Wolfenstein parameters along with $C_T$ for the NP scale $\Lambda = 5$ TeV.

| $\Lambda = 5$ TeV | $C_T$ | A | $\lambda$ | $\bar{\rho}$ | $\bar{\eta}$ |
|---|---|---|---|---|---|
| $C_T$ | 1. | −0.00275994 | −0.000450748 | 0.00303057 | 0.00405182 |
| A | −0.00275994 | 1. | −0.258676 | −0.212262 | −0.494841 |
| $\lambda$ | −0.000450748 | −0.258676 | 1. | 0.0715675 | −0.0577073 |
| $\bar{\rho}$ | 0.00303057 | −0.212262 | 0.0715675 | 1. | 0.406381 |
| $\bar{\eta}$ | 0.00405182 | −0.494841 | −0.0577073 | 0.406381 | 1. |

TABLE XV. Similar to Table I including the data set from the Belle 2017 analysis [43].

| | Fit quality | | | |
|---|---|---|---|---|
| Data set | $\chi^2$/d.o.f. | $p$-value | Parameter | Fit result |
| Belle 2017 [43] + Belle 2018 [40] + $h_{A_1}(1)$ [42] + LCSR [41] + lattice [38] | 101.66/85 | 10.5% | $\lvert V_{cb}\rvert$ | $38.55(70) \times 10^{-3}$ |
| | | | $a_0^f$ | 0.0123(1) |
| | | | $a_1^f$ | 0.0192(95) |
| | | | $a_2^f$ | −0.460(194) |
| | | | $a_0^g$ | 0.0319(10) |
| | | | $a_1^g$ | −0.140(62) |
| | | | $a_2^g$ | −0.25(145) |
| | | | $a_1^{\mathcal{F}_1}$ | 0.0021(15) |
| | | | $a_0^{\mathcal{F}_2}$ | 0.0517(12) |
| | | | $a_1^{\mathcal{F}_2}$ | −0.160(59) |
| | | | $a_2^{\mathcal{F}_2}$ | 0.986(916) |

TABLE XVI. Fit results similar to those in Table VI by additionally including the Belle 2017 data set.

| Case | | | | Fit result | | | |
|---|---|---|---|---|---|---|---|
| | $\chi^2$/d.o.f. | $p$-value (%) | $C_T$ (GeV$^{-2}$) | A | $\lambda$ | $\bar{\rho}$ | $\bar{\eta}$ |
| Scale 1 TeV | 140.5/110 | 3 | $0.00003 \pm 0.00013$ | $0.795114 \pm 0.007472$ | $0.224979 \pm 0.000293$ | $0.17781 \pm 0.00973$ | $0.390305 \pm 0.011842$ |
| Scale 2 TeV | 140.5/110 | 3 | $0.00002 \pm 0.00009$ | $0.795112 \pm 0.007472$ | $0.224979 \pm 0.000293$ | $0.177811 \pm 0.009728$ | $0.390305 \pm 0.011842$ |
| Scale 5 TeV | 140.5/110 | 3 | $0.000015 \pm 0.000066$ | $0.795112 \pm 0.007472$ | $0.224979 \pm 0.000293$ | $0.177811 \pm 0.009728$ | $0.390305 \pm 0.011842$ |

[1] J. Abdallah *et al.*, arXiv:1409.2893.
[2] J. Abdallah *et al.*, Phys. Dark Universe **9–10**, 8 (2015).
[3] A. De Simone and T. Jacques, Eur. Phys. J. C **76**, 367 (2016).
[4] C. Englert, M. McCullough, and M. Spannowsky, Phys. Dark Universe **14**, 48 (2016).
[5] A. Albert *et al.*, Phys. Dark Universe **16**, 49 (2017).
[6] O. Buchmueller, A. De Roeck, K. Hahn, M. McCullough, P. Schwaller, K. Sung, and T.-T. Yu, J. High Energy Phys. 09 (2017) 076.
[7] D. Schmeier, Other thesis, 2013, arXiv:1308.4409.
[8] A. Greljo, J. Julio, J. F. Kamenik, C. Smith, and J. Zupan, J. High Energy Phys. 11 (2013) 190.
[9] S. Matsumoto, Y.-L. S. Tsai, and P.-Y. Tseng, J. High Energy Phys. 07 (2019) 050.
[10] T. Li, J. High Energy Phys. 04 (2017) 112.
[11] T. Li, Phys. Lett. B **782**, 497 (2018).
[12] E. Morgante, Adv. High Energy Phys. **2018**, 5012043 (2018).
[13] C. Arina, E. Del Nobile, and P. Panci, Phys. Rev. Lett. **114**, 011301 (2015).
[14] C. Arina *et al.*, J. High Energy Phys. 11 (2016) 111.
[15] M. Bauer, M. Neubert, and A. Thamm, Phys. Rev. Lett. **117**, 181801 (2016).
[16] M. J. Dolan, F. Kahlhoefer, C. McCabe, and K. Schmidt-Hoberg, J. High Energy Phys. 03 (2015) 171; 07 (2015) 103(E).
[17] G. Arcadi, M. Dutra, P. Ghosh, M. Lindner, Y. Mambrini, M. Pierre, S. Profumo, and F. S. Queiroz, Eur. Phys. J. C **78**, 203 (2018).
[18] J. M. No, Phys. Rev. D **93**, 031701 (2016).
[19] G. Arcadi, M. Lindner, F. S. Queiroz, W. Rodejohann, and S. Vogl, J. Cosmol. Astropart. Phys. 03 (2018) 042.
[20] N. F. Bell, G. Busoni, and I. W. Sanderson, J. Cosmol. Astropart. Phys. 08 (2018) 017; 01 (2019) E01.
[21] R. Flores, K. A. Olive, and S. Rudaz, Phys. Lett. B **232**, 377 (1989).
[22] N. F. Bell, J. B. Dent, A. J. Galea, T. D. Jacques, L. M. Krauss, and T. J. Weiler, Phys. Lett. B **706**, 6 (2011).
[23] N. F. Bell, J. B. Dent, T. D. Jacques, and T. J. Weiler, Phys. Rev. D **84**, 103517 (2011).
[24] N. F. Bell, Y. Cai, J. B. Dent, R. K. Leane, and T. J. Weiler, Phys. Rev. D **96**, 023011 (2017).
[25] J. Kumar, J. Liao, and D. Marfatia, Phys. Lett. B **759**, 277 (2016).
[26] S. J. Clark, J. B. Dent, B. Dutta, and L. E. Strigari, Phys. Rev. D **99**, 083003 (2019).

[27] Y. S. Amhis *et al.* (HFLAV Collaboration), Eur. Phys. J. C **81**, 226 (2021).

[28] P. A. Zyla *et al.* (Particle Data Group), Prog. Theor. Exp. Phys. **2020**, 083C01 (2020).

[29] P. Gambino and C. Schwanda, Phys. Rev. D **89**, 014022 (2014).

[30] A. Alberti, P. Gambino, K. J. Healey, and S. Nandi, Phys. Rev. Lett. **114**, 061802 (2015).

[31] P. Gambino, K. J. Healey, and S. Turczyk, Phys. Lett. B **763**, 60 (2016).

[32] Results on Time-Dependent *CP* Violation and Measurements Related to the Angles of the Unitarity Triangle: Winter conferences (Moriond, etc.) and PDG 2021, https://hflav.web.cern.ch/content/unitary-triangle-angles.

[33] B. Batell, M. Pospelov, and A. Ritz, Phys. Rev. D **83**, 054005 (2011).

[34] M. Freytsis, Z. Ligeti, and J. Thaler, Phys. Rev. D **81**, 034001 (2010).

[35] Y. Sakaki, M. Tanaka, A. Tayduganov, and R. Watanabe, Phys. Rev. D **88**, 094012 (2013).

[36] S. Jaiswal, S. Nandi, and S. K. Patra, J. High Energy Phys. 12 (2017) 060.

[37] S. Jaiswal, S. Nandi, and S. K. Patra, J. High Energy Phys. 06 (2020) 165.

[38] A. Bazavov *et al.* (Fermilab Lattice, MILC Collaborations), Eur. Phys. J. C **82**, 1141 (2022).

[39] C. G. Boyd, B. Grinstein, and R. F. Lebed, Phys. Rev. D **56**, 6895 (1997).

[40] E. Waheed *et al.* (Belle Collaboration), Phys. Rev. D **100**, 052007 (2019); **103**, 079901(E) (2021).

[41] N. Gubernari, A. Kokulu, and D. van Dyk, J. High Energy Phys. 01 (2019) 150.

[42] J. A. Bailey *et al.* (Fermilab Lattice, MILC Collaborations), Phys. Rev. D **89**, 114504 (2014).

[43] A. Abdesselam *et al.* (Belle Collaboration), arXiv:1702.01521.

[44] D. Bigi, P. Gambino, and S. Schacht, J. High Energy Phys. 11 (2017) 061.

[45] http://ckmfitter.in2p3.fr/www/results/plots_summer19/num/ckmEval_results_summer19.html.

[46] J. Charles *et al.*, Phys. Rev. D **91**, 073007 (2015).

[47] J. Charles *et al.*, Phys. Rev. D **84**, 033005 (2011).

[48] J. Charles, A. Hocker, H. Lacker, S. Laplace, F. R. Le Diberder, J. Malcles, J. Ocariz, M. Pivk, and L. Roos (CKMfitter Group), Eur. Phys. J. C **41**, 1 (2005).

[49] J. Hardy and I. Towner, in *Proceedings of the 13th Conference on the Intersections of Particle and Nuclear Physics* (2018), arXiv:1807.01146.

[50] M. Moulson, Proc. Sci. CKM2016 (**2017**) 033.

[51] A. Biswas, S. Nandi, S. K. Patra, and I. Ray, J. High Energy Phys. 07 (2021) 082.

[52] A. Biswas and S. Nandi, J. High Energy Phys. 09 (2021) 127.

[53] B. Capdevila, P. Gambino, and S. Nandi, J. High Energy Phys. 04 (2021) 137.

[54] M. Bordone, B. Capdevila, and P. Gambino, Phys. Lett. B **822**, 136679 (2021).

[55] R. Aaij *et al.* (LHCb Collaboration), Nat. Phys. **11**, 743 (2015).

[56] A. M. Sirunyan *et al.* (CMS Collaboration), J. High Energy Phys. 04 (2020) 188.

[57] R. Aaij, J. High Energy Phys. 12 (2016) 087.

[58] G. Aad *et al.* (CMS, ATLAS Collaborations), J. High Energy Phys. 08 (2020) 051.

[59] S. Aoki *et al.* (Flavour Lattice Averaging Group), Eur. Phys. J. C **80**, 113 (2020).

[60] CKMfitter global fit results as of Summer 19, http://ckmfitter.in2p3.fr/www/results/plots_summer19/num/ckmEval_results_summer19.pdf.

[61] F. Déliot, R. Faria, M. C. N. Fiolhais, P. Lagarelhos, A. Onofre, C. M. Pease, and A. Vasconcelos, Phys. Rev. D **97**, 013007 (2018).

[62] F. Déliot, M. C. N. Fiolhais, and A. Onofre, Mod. Phys. Lett. A **34**, 1950142 (2019).

[63] M. Jung and D. M. Straub, J. High Energy Phys. 01 (2019) 009.

[64] U. Haisch and E. Re, J. High Energy Phys. 06 (2015) 078.

[65] E. Aprile *et al.* (XENON Collaboration), Phys. Rev. Lett. **121**, 111302 (2018).

[66] G. Aad *et al.* (ATLAS Collaboration), Phys. Rev. D **103**, 112006 (2021).

[67] A. M. Sirunyan *et al.* (CMS Collaboration), Phys. Rev. Lett. **122**, 011803 (2019).

[68] A. M. Sirunyan *et al.* (CMS Collaboration), J. High Energy Phys. 04 (2019) 031.

[69] A. M. Sirunyan *et al.* (CMS Collaboration), J. High Energy Phys. 03 (2019) 141.

[70] A. Tumasyan *et al.* (CMS Collaboration), J. High Energy Phys. 11 (2021) 153.

[71] D. Abercrombie *et al.*, Phys. Dark Universe **27**, 100371 (2020).